

# Important Notice

This copy may be used only for the purposes of research and private study, and any use of the copy for a purpose other than research or private study may require the authorization of the copyright owner of the work in question. Responsibility regarding questions of copyright that may arise in the use of this copy is assumed by the recipient.

UNIVERSITY OF CALGARY

Evaluation of the seismic reflection method as a monitoring tool during primary and  
enhanced coalbed methane production

by

Diane Jael Lespinasse Fung

A THESIS

SUBMITTED TO THE FACULTY OF GRADUATE STUDIES  
IN PARTIAL FULFILMENT OF THE REQUIREMENTS FOR THE  
DEGREE OF MASTER OF SCIENCE

DEPARTMENT OF GEOSCIENCE

CALGARY, ALBERTA

APRIL, 2012

© Diane Jael Lespinasse Fung 2012

UNIVERSITY OF CALGARY  
FACULTY OF GRADUATE STUDIES

The undersigned certify that they have read, and recommend to the Faculty of Graduate Studies for acceptance, a thesis entitled " Evaluation of the seismic reflection method as a monitoring tool during primary and enhanced coalbed methane production" submitted by Diane Jael Lespinasse Fung in partial fulfilment of the requirements of the degree of Master of Science.

---

*Supervisor, Dr. Robert J. Ferguson  
Department of Geoscience*

---

*Dr. Laurence R. Lines  
Department of Geoscience*

---

*Dr. Cristian Rios  
Department of Mathematics and Statistics*

---

*Date*

## Abstract

In this thesis I present an evaluation of the seismic reflection method as a monitoring tool during coalbed methane (CBM) production and enhanced coalbed methane (ECBM) production by CO<sub>2</sub> injection. This evaluation is based on a workflow previously developed for monitoring CO<sub>2</sub> storage in the Big George coalbeds in the Powder River Basin.

I study the changes in seismic and the AVO response associated with coalbeds during primary production using a data set from the Mannville coals, which represent one of the most important CBM resources in the Province of Alberta. Using published data, I perform a single well flow simulation to make an assessment of its production forecast in a 10 year period. The flow simulation provides information on methane saturation and reservoir pressure during production, while the changes in porosity and permeability due to depletion are estimated according to the Palmer and Mansoori permeability model. Using well log data of the Corbett Field and the results of the flow simulation, I complete a Gassmann fluid substitution to replace brine by a mixture of brine and methane in the pore space and estimate the variations in  $V_p$ ,  $V_s$  and density due to changes in fluid saturation. I evaluate offset dependent synthetic seismograms before and after fluid substitution, and I use different coalbed thicknesses to establish resolution limits. To observe significant changes in the character and phase of the wavelet due to the replacement of brine by methane I find that coalbed thickness must be at least 10 m, also in terms of AVO I observe that there is a decrease in amplitude with offset caused by the presence of methane in the pore space.

Using the same methodology and production data from the Fruitland Coals Fairway in the North of the San Juan Basin U.S.A, which is considered the most productive CBM reservoir in the world, I evaluate Elastic Impedance (EI) and Elastic Impedance Coefficient (EC) response during ECBM by CO<sub>2</sub> injection. In this case, I determine that EI and EC are not able to discriminate CO<sub>2</sub> from methane but they do allow monitoring the movement of the CO<sub>2</sub> flood during and after injection. The magnitude of the changes of EI, and EC are small, and it is difficult to predict whether the changes will be appreciated in seismic data.

## **Acknowledgements**

I would like to thank my supervisor Dr. Robert J. Ferguson for his support and guidance during the development of this thesis. Thank you for your advice and for encouraging me to give my best in every step of my Master program.

Thanks you Dr. Christopher Clarkson, for introducing me to the fluid simulation world and for sharing your knowledge with me. Without your contributions this work would not be possible.

Thank you Dr. Laurence Lines, for your continuous support of my work and for always being available for help. Dr. Don Lawton, thanks for your valuable comments and advice.

Thanks you Jason McCrank for your advice and for being so helpful. Thanks for your rapid response to all my questions and for your disposition to help.

A special thanks you to Faranak Mahmoudian and Mahdi Al-Mutlaq for being amazing officemates and for sharing your experience with me. Thanks for all those valuable comments and suggestions that helped me to improve my work.

I also would like to thank you my CREWES fellows Melissa Hernandez, Hassan Khaniani, Heather Lloyd, Virginia Vera, Vanja Vracar, Steve Kim and Peter Gagliardi for all those wonderful moments we shared during my university days and helping it becomes a wonderful and rewarding experience.

A special thanks you to Kevin Hall who patiently helped me to overcome all the technical difficulties that I found during my stay in CREWES and to Rolf Maier for his suggestions.

Thanks you CREWES for giving me the opportunity to come to Calgary and be part of this incredible group. Thanks you to CREWES staff, especially Laura Baird for taking care of us.

I also would like to thank my mom, my dad and my brother for the encouraging words they gave me when I most needed them, and for your unconditional support. You have always been very supportive of me, and I love you all very much

Finally, Julian Ferreira, thanks for your patience and support in these last months. Thank you for sharing this experience with me and for taking care of me.

## **Dedication**

To my mom, my dad and, my brother, with love

## Table of Contents

Approval Page.....	ii
Abstract.....	iii
Acknowledgements.....	v
Dedication.....	vii
Table of Contents.....	viii
List of Tables.....	xi
List of Figures.....	xii
List of Symbols and Abbreviations.....	xv
Chapter 1. Introduction.....	1
1.1 CBM in the USA.....	2
1.2 CBM in Canada.....	3
1.3 CBM around the world.....	4
1.4 Previous work on CBM.....	6
1.5 Thesis objectives.....	8
1.6 Thesis outline.....	9
Chapter 2. Theoretical development.....	11
2.1 Coalbed Methane (CBM).....	11
2.1.1 CBM production.....	12
2.1.2 Enhanced coalbed methane.....	13
2.1.3 Changes in the coal matrix due to CBM and CO <sub>2</sub> -ECBM production.....	15
2.2 Coal permeability modelling.....	17
2.2.1 Langmuir Isotherm.....	17
2.2.2 Palmer and Mansoori permeability model.....	19
2.3 Fluid substitution and Gassmann's equation.....	20
2.4 Elastic Impedance.....	22
Chapter 3. Evaluation of the seismic response of coalbeds. 1D analysis. Mannville coals, Corbett field, Alberta Canada.....	25

3.1	Area of study.....	25
3.1.1	Mannville Group.....	28
3.1.2	Corbett Creek coal properties .....	29
3.2	Methodology.....	30
3.2.1	Data set selection and data collection .....	30
3.2.2	Fluid simulation .....	31
3.2.2.1	Construction of the Langmuir isotherm.....	32
3.2.2.2	Matrix shrinkage/swelling .....	33
3.2.2.3	Deliverability and production forecast.....	34
3.2.2.4	Shear wave velocity estimation .....	35
3.2.3	Fluid properties .....	35
3.2.3.1	Gas .....	35
3.2.3.2	Brine.....	37
3.2.4	Gassmann fluid substitution.....	39
3.2.5	Synthetic seismograms.....	42
3.3	Results.....	43
3.3.1	Fluid simulation .....	43
3.3.2	Synthetic seismograms.....	46
3.3.2.1	Case I: Corbett Field .....	46
3.3.2.2	Case II: Coal seam with a thickness of 10.64 m.....	50
3.3.2.3	Case III: Coal seam with a thickness of 21.28 m.....	50
3.3.3	CREWES Zoeppritz equation .....	53
3.4	Summary.....	57
 Chapter 4. Elastic Impedance analysis for methane and CO <sub>2</sub> discrimination in coalbeds. Fruitland coals, San Juan Basin .....		
4.1	Area of study.....	58
4.1.1	Fruitland Formation .....	60
4.2	Methodology.....	62
4.2.1	Fluid simulation .....	62
4.2.2	Data selection.....	64
4.2.3	Gassmann fluid substitution.....	66
4.3	Results.....	69

4.3.1 Fluid simulation .....	69
4.3.2 Gassmann fluid substitution.....	72
4.3.3 Impedance analysis .....	76
4.4 Summary.....	78
Chapter 5. Conclusions.....	80
5.1 Evaluation of time-lapse seismic as a monitoring tool during CBM production ..	80
5.2 Evaluation of Elastic Impedance and Elastic Impedance Coefficient as a monitoring tool during CO <sub>2</sub> -ECBM production .....	81
References.....	83

## List of Tables

Table 1 Reservoir and pore fluid parameters .....	32
Table 2. Methane Langmuir parameters .....	32
Table 3. Parameters for the Palmer and Mansoori model.....	33
Table 4. Constants for the water velocity calculation (Batzie and Wang, 1992).....	38
Table 5. Data used for gas properties calculation .....	39
Table 6. Fluid properties at reservoir conditions. ....	39
Table 7. Water saturation variation with pressure .....	46
Table 8. Parameters for CREWES Zoeppritz explorer.....	56
Table 9. Langmuir parameters .....	63
Table 10. Reservoir model assumptions .....	63
Table 11. $V_p$ , $V_s$ and density selected values.....	66

## List of Figures

Figure 1. Cleat system in coalbeds. ....	12
Figure 2. Methane desorption from a coal matrix. As reservoir pressure decreases as a consequence of water production, methane desorbs from the coal matrix. ....	14
Figure 3. Coal matrix shrinkage due to methane desorption. ....	16
Figure 4. Corbett Field and 100-03-22-062-06W500 well location. ....	26
Figure 5. Well log of the well 100-03-22-062-06W500. a) Compensated density log, b) compensated sonic log.....	27
Figure 6. Tank model assumed for fluid simulation. This model establishes that the properties of the reservoir do not vary from point to point, hence an average of the properties is used.....	31
Figure 7. Desorption isotherm. This curve determines the methane desorbed from the coal matrix at a specific reservoir pressure.....	33
Figure 8. Relative permeability curves. ....	34
Figure 9. 30 Hz and 60 Hz Ricker wavelets for synthetic seismograms. ....	43
Figure 10. Variation of the porosity ratio with the reservoir pressure, estimated with model due to Palmer and Mansoori (1998).....	44
Figure 11. Gas and water production forecast. This graph provides an estimation of the gas and water production per day along a 10 years period, starting the first day of production. ....	45
Figure 12. Synthetic seismograms for two coal seams (Main and Lower seam), generated with a 30 Hz zero phase Ricker wavelet. a) coalbeds are saturated with 100% brine, b) coalbeds are saturated with 82% brine and 18% methane. ....	48
Figure 13. Synthetic seismograms for two coal seams (Main and Lower seam), generated with a 60 Hz zero phase Ricker wavelet. a) coalbeds are saturated with 100% brine, b) coalbeds are saturated with 82% brine and 18% methane. ....	49
Figure 14. Synthetic seismograms for a 10.61 m coalbed, generated with a 30 Hz zero phase Ricker wavelet. a) coalbeds are saturated with 100% brine, b) coalbeds are saturated with 82% brine and 18% methane.....	51
Figure 15. Synthetic seismograms for a 10.61 m coalbed. Generated with a 60 Hz zero phase Ricker wavelet. a) coalbeds are saturated with 100% brine, b) coalbeds are saturated with 82% brine and 18% methane.....	52

Figure 16. Depth domain synthetic seismograms for a 21.28 m coalbed, generated with a 30 Hz zero phase Ricker wavelet. a) coalbeds are saturated with 100% brine, b) coalbeds are saturated with 82% brine and 18% methane.....	54
Figure 17. Synthetic seismograms for a 21.28 m coalbed, generated with a 60 Hz zero phase Ricker wavelet. a) coalbeds are saturated with 100% brine, b) coalbeds are saturated with 82% brine and 18% methane.....	55
Figure 18. CREWES Zoeppritz explorer (CREWES.org). Upper layer corresponds to an average of the overburden parameters and the lower layer is the coalbed.....	56
Figure 19. San Juan Basin map. Red line shows the limits of the Fruitland Fairway. ....	59
Figure 20. Depositional sequence of the Upper Cretaceous in the San Juan Basin.....	61
Figure 21. $V_p$ , $V_s$ and density model from the Hamilton 3 well, Cedar Hill, San Juan Basin (Figure 8, Ramos and Davis, 1997). ....	64
Figure 22. Density logs. Pump Canyon, San Juan Basin (Modified from Figure 5, Koperma et al., 2009).....	65
Figure 23. Dependence of the mineral matrix bulk modulus with $\epsilon$ and $\phi$ a) using maximum $V_p$ value associated with coals, b) using minimum $V_p$ value associated with coals. ....	67
Figure 24. Dependence of the mineral matrix bulk modulus with $\epsilon$ and the $\phi$ a) using $V_p$ , $V_s$ and density values associated with the San Juan Basin, b) comparison of the three surfaces (maximum $V_p$ , minimum $V_p$ , San Juan Basin data). ....	68
Figure 25. Reservoir pressure. a) Primary production (2002), b) ECBM by $\text{CO}_2$ injection (2005), and c) one year after shutting the injection wells (2011). ....	71
Figure 26. Methane saturation. a) Primary production (2002), b) ECBM by $\text{CO}_2$ injection (2005), and c) one year after shutting the injection wells (2011). ....	71
Figure 27. $\text{CO}_2$ saturation a) Primary production (2002); b) ECBM by $\text{CO}_2$ injection (2005), and c) one year after shutting the injection wells (2011). ....	73
Figure 28. Water saturation. a) Primary production (2002); b) ECBM by $\text{CO}_2$ injection (2005), and c) one year after shutting the injection wells (2011). ....	73
Figure 29. $V_p$ a) Primary production (2002), b) ECBM by $\text{CO}_2$ injection (2005), and c) one year after shutting the injection wells (2011).....	74
Figure 30. $V_s$ a) Primary production (2002), b) ECBM by $\text{CO}_2$ injection (2005), and c) one year after shutting the injection wells (2011).....	74

Figure 31. Bulk density a) Primary production (2002), b) ECBM by CO<sub>2</sub> injection (2005), and c) one year after shutting the injection wells (2011). ..... 75

Figure 32. EI a) Primary production (2002), b) ECBM by CO<sub>2</sub> injection (2005), and c) one year after shutting the injection wells (2011)..... 77

Figure 33. EC a) Primary production (2002), b) ECBM by CO<sub>2</sub> injection (2005), and c) one year after shutting the injection wells (2011)..... 77

## List of Symbols and Abbreviations

<b>Symbol</b>	<b>Definition</b>
AI	Acoustic Impedance
AVO	Amplitude versus offset
bcf/d	Billion cubic feet per day
bcf/section	Billion cubic feet per section
°C	Celsius degrees
CBM	Coalbed methane
CH <sub>4</sub>	Methane
$C_f/\phi_i$	Fracture compressibility
cm	Centimeters
cm <sup>3</sup> /g	Cubic centimeters per gram
CO <sub>2</sub>	Carbon dioxide
CO <sub>2</sub> -ECBM	Enhanced coalbed methane by CO <sub>2</sub> injection
CREWES	Consortium for Research in Elastic Wave Exploration Seismology
DOE	Department of Energy
EC	Elastic Impedance Coefficient
ECBM	Enhanced coalbed methane
EI	Elastic Impedance
ft	Feet
G	Specific gravity
g/cm <sup>3</sup>	Grams per cubic centimeters
GPa	Gigapascal
Hz	Hertz
$k$	Permeability
K	Bulk modulus
$K_0$	Bulk modulus of the mineral matrix
$K^*$	Bulk modulus of the frame of the rock (dry rock)
$K_{\text{brine}}$	Bulk modulus of brine
$K_{\text{CH}_4}$	Bulk modulus of methane
$K_{\text{fl}}$	Bulk modulus of the fluids in the pore space
Kg/m <sup>3</sup>	Kilograms per cubic meter
$k_i$	Initial permeability
km <sup>2</sup>	Square kilometers
km/s	Kilometers per second
KPa	Kilopascal
$K_s$	Bulk modulus of a gas at adiabatic conditions
$K_{\text{sat}}$	Bulk modulus of the saturated rock
m	Meter
M	Constrained axial modulus
mcf/d	Thousand cubic feet per day
mD	MilliDarcy

$m^3/d$	Cubic meters per day
mmcf/d	Million cubic feet per day
MPa	Megapascal
m/s	Meters per second
$N_2$	Nitrogen
NE	North east
nm	Nanometer
NW	North west
P	Pressure
$P_i$	Initial reservoir pressure
$P_L$	Langmuir pressure
$P_L CH_4$	Langmuir pressure for methane
$P_L CO_2$	Langmuir pressure for carbon dioxide
ppm	Parts per million
$P_{pr}$	Pseudo-reduced pressure
psia	Pound per square inch absolute
R	Gas constant
S	Salinity
scf/ton	Standard cubic feet per ton
SEM	Scanning electron microscopy
SW	South west
T	Temperature
$T_a$	Absolute temperature
Tcf	Trillion cubic feet
$T_{pr}$	Pseudo-reduced temperature
USBM	United States Bureau of Mines
V	Adsorbed volume of gas
$V_b$	Brine velocity
$V_w$	Water velocity
$V_L$	Langmuir volume
$V_L CH_4$	Langmuir volume for methane
$V_L CO_2$	Langmuir volume for carbon dioxide
$V_p$	Compressional wave velocity
$V_s$	Shear wave velocity
wt%	Percentage in weight
X-ray CT	X-ray computed tomography
Z	Compressibility factor
%	Percentage

### Greek Symbols

$\beta$	Grain compressibility
$\gamma_0$	Heat capacity
$\epsilon_\infty$	Volumetric strain at infinite pressure
$\mu$	Shear modulus

$\phi$	Porosity
$\phi_{\text{brine}}$	Fraction of brine
$\phi_{\text{CH}_4}$	Fraction of methane
$\phi_i$	Initial porosity
$\rho$	Density
$\rho_b$	Bulk density
$\rho_B$	Brine density
$\rho_{\text{CH}_4}$	Density of methane
$\rho_{\text{flmix}}$	Density of a mix of fluid
$\rho_g$	Matrix density
$\rho_w$	Water density
$\theta$	Angle of incidence

## **Chapter 1. Introduction**

In general, coal is defined as a sedimentary rock in which the percentage (in weight) of organic matter is bigger than the percentage of inorganic matter. More specifically and with the intention to differentiate organic shales from coals, it is established that coals have a percentage in weight of organic matter >50 wt% (Alpern and Sousa, 2002). Methane in coals is originated by processes of geochemical and bacterial character that affected the organic matter during the coalification process (Jenkins et al., 2008).

In the past, gases emitted from coals have been considered an important problem that put to risk a significant number of people during mining operations (Morad et al., 2008). The need of draining these gases from the coalbed brought about the implementation of a degasification process of coal mines by drilling horizontal and vertical wells in the coalbed, and this awakened the interest in the production of coalbed methane (CBM) (Clarkson and Bustin, 2010).

CBM has become a significant source of natural gas (Morad et al., 2008) due to its capacity to produce and store large amounts of methane (Beaton et al., 2006), and for its potential as a source of clean energy (Shi and Durucan, 2005). Coalbed methane is the term that defines the gas that is produced in coalbeds during its formation process (Gatens, 2005) and consists mainly of methane accompanied by smaller proportions of CO<sub>2</sub> and nitrogen (Clarkson and Bustin, 2000). CBM is classified as an unconventional resource because of its nature of being source and reservoir at the same time, its low permeability (McCrank and Lawton, 2009), and the mechanisms of gas storage among other characteristics (Bell and Rakop, 1986).

CBM production is achieved by lowering the reservoir pressure to generate methane desorption (McCrank and Lawton, 2009). This technique makes possible the recovery of approximately 50% of the gas in the coalbed (Clarkson and Bustin, 2010); therefore enhanced coalbed methane (ECBM) techniques emerge to improve the methane recovery rates. One of the most relevant ECBM techniques is the injection of CO<sub>2</sub> in the coalbed to help reduce this greenhouse gas in the atmosphere (McCrank and Lawton, 2009).

Since conventional gas production has decreased, unconventional resources are being evaluated as energy sources for the future (Gatens, 2005). The CBM reserves in the world are around 9000 Tcf and represent a great potential energy supply. During the last two decades, the CBM industry has rapidly grown and important advances in reservoir characterization, well completion techniques, production, and production costs has been achieved (Jenkins et al., 2008). However, the development and growth of the CBM industry will strongly depend on the prices and production rate of natural gas from conventional reservoirs (Flaim et al., 1987).

### **1.1 CBM in the USA**

The CBM production with commercial purposes started in the 1980`s in the USA. Initially the efforts were directed to improve safety in mining operations but an increase in the price of the natural gas made the commercial production of CBM the new target (Gatens, 2005).

In the USA, significant amounts of money were dedicated to CBM research projects and financial benefits were offered by the government (Gatens, 2005). The financial benefits were based on a tax credit program known as “Crude oil windfall profit tax” for unconventional resources (Clarkson and Bustin, 2010). This program promotes the

investment in alternative sources of energy in the USA, and more specifically from unconventional reservoirs like tight sands, CBM, organic shales, etc. (Gatens, 2005). The tax credit applied to all wells that drilled after 1979 and before December 1992; hence, during this period an important increase in the number of completed CBM wells is observed (Byrnes and Schuldhaus, 1995)

Lately, the CBM industry has grown and the estimated reserves of CBM in the USA are around 700 Tcf (Morad et al., 2008). By 2010, the daily production had reached 20 bcf/d which correspond to approximately 8% of the total natural gas production in the USA (Clarkson and Bustin, 2010). The CBM production is the result of more 40000 wells that has been completed in more than 20 basins (Jenkins et al., 2008), with the San Juan Basin (Colorado and New Mexico), the Powder River Basin (Wyoming and Montana), and the Black Warrior Basin (Alabama) being the more developed ones (Morad et al., 2008).

Since the 1990, the San Juan Basin became the most important CBM producer in the world with single wells producing 1-6 mmcf/day (Beaton et al., 2006). The most productive area in the San Juan Basin is the Fruitland Formation Fairway, where the overpressure of the area, the high permeability and the coals with bituminous rank contribute with the excellent conditions for CBM production (Beaton et al., 2006). The success of the San Juan Basin in CBM production caught the attention of the world starting the development of several exploration and production projects (Clarkson and Bustin, 2010) in countries like Canada and Australia (Jenkins et al., 2008).

## **1.2 CBM in Canada**

CBM accumulations in Canada can be found in British Columbia, Saskatchewan, Nova Scotia, the Northwest Territories, Yukon, and the Western Canadian Sedimentary

Basin which is the largest one (Gatens, 2005). The Province of Alberta possesses a great amount of CBM resources including the Mannville coals (with the highest concentration of CBM), the Belly River, the Horseshoe Canyon, and the Ardley coals (Beaton et al., 2006).

Based on the success of the USA on CBM production, Canada started its incursion in this industry by the end of the 1980's (Beaton et al., 2006). Since then and until 2000, approximately 200 wells were unsuccessfully completed causing a decrease in the interest for CBM. Even though the coals presented high gas accumulation, the permeability was too low to affect the production rates (Gatens, 2005). Later on, the prediction of scarcity of energy supplies in the future and better gas prices brings back the attention to CBM. The exploration activity restarts (Beaton et al., 2006) and in 2003 commercial CBM production was reached in the coals of the Horseshoe Canyon Formation, Alberta (Gatens, 2005). This is the first success in commercial CBM production that occurs outside the USA (Clarkson and Bustin, 2010). Nowadays, CBM projects are being developed in the Mannville and the Ardley coals along the Province of Alberta (Beaton et al., 2006).

By 2008, the Canadian CBM resources are estimated to be around 700 Tcf of which approximately 550 Tcf are in Alberta, and 90 Tcf are in the British Columbia. Today more than 3900 wells for CBM production has been completed in Canada (Gatens, 2005) producing approximately 1 Bcf/d by 2010 (Clarkson and Bustin, 2010). Of the total CBM production 90% or more comes from the Horseshoe Canyon coals (Clarkson and Bustin, 2010).

### **1.3 CBM around the world**

The exploration and production of CBM has slowly extended outside North America (Jenkins et al., 2008) and in several countries the exploration activity is reduced.

Currently, 14 countries have been identified as having the largest reserves of CBM in the world, including: Russia, China, United States, Australia, Canada, Indonesia, South Africa, Ukraine, Turkey, and India among others (Clarkson and Bustin, 2010). The CBM reserves are estimated to be about 9000 Tcf (Jenkins et al., 2008) of which around 90% belongs to Russia Canada, China and the USA (Lin et al., 2008).

In Russia, as a consequence of the abundant reserves of natural gas from conventional reservoirs, CBM has received little attention. In this country the potential production areas are widely unexplored, limiting development activities (Clarkson and Bustin, 2010). In the case of China, the resources of CBM are estimated in 1200 Tcf, but it is difficult to estimate the percentage of recoverable gas (Chakhmakhchev, 2007). In addition, the CBM production has been limited to the methane production that is part of the degasification process of coal mines and that precedes the mining operations (Clarkson and Bustin, 2010). Countries like Vietnam and Mongolia do not have the technology and the infrastructure to start CBM exploration and development. Therefore, these two countries have made agreements with companies from Canada to initiate CBM operations (Chakhmakhchev, 2007).

Recently, the most important CBM development took place in Queensland, Australia, reaching a production  $> 1$  mmcf/day by implementing horizontal and vertical well developments (Clarkson and Bustin, 2010). After USA and Canada, Australia can be considered the country with the most developed CBM industry. In this country, approximately 30 basins with potential for CBM production have been identified and the proven CBM reserves ascend to 9 Tcf (Chakhmakhchev, 2007).

#### **1.4 Previous work on CBM**

The CBM industry has been growing and important advances in exploration, production and the development of technology have been achieved (Jenkins et al., 2008). Thanks to these advances, CBM has become an important source of natural gas and studies that aim to determine the physical properties of coals and monitor coalbed methane primary and enhance production are increasingly important.

As an unconventional resource, it is important to understand the characteristics of CBM reservoirs as well as the complexities associated with them. Morad et al. (2008) present a summary of the coal rank classification and gives an introduction to the porosity systems that control the fluid flow in this kind of reservoirs. This work also shows an overview of the storage and transport mechanisms that take place in coalbeds as well as a comparison between CBM reservoirs and conventional reservoirs. Jenkins et al. (2008) also present the fundamentals of CBM reservoirs, and evaluate the existence and required technology for profitable CBM production.

The adsorption capacity is an important characteristic in coalbeds since it represents the principal storage mechanism in coals and causes the coal matrix deformation (Robertson and Christiansen, 2007). Karacan (2007) presents results in which he explains how the adsorption and desorption of gases can cause swelling or shrinkage of the coal matrix and the associated consequences. In his paper, he evaluates the internal changes suffered by a coal sample in presence of CO<sub>2</sub>. In this case the changes in the internal structure of the coal are studied by using scanning electron microscopy (SEM) and dual-energy X-ray computed tomography (X-ray CT). Balan and Gumrah (2009) also study the changes in the coal matrix due to gas sorption and present a methodology to produce more

accurate fluid simulations based on the coal properties and the coal rank. Different reservoir conditions are evaluated including changes in the reservoir due to  $N_2$  and  $CO_2$  adsorption during ECBM production.

The changes in the coal matrix due to gas sorption bring as a consequence variations in the porosity and permeability of the coal, which is key factor for CBM and ECBM production (Robertson and Christiansen, 2007). Several models have been developed to estimate these changes in coalbeds. Palmer and Mansoori (1998) generate a permeability model for coals that takes into account the changes in porosity and permeability caused by matrix deformation and changes in the effective stress while Shi and Durucan (2005) formulated a permeability model that relates the changes in the volumetric strain in the coal matrix with the quantity of gas that is desorbed. Palmer (2009) presents a comparison of the most used permeability models for coals. In this comparison he includes his own model, the Shi and Durucan (2005) model, and the Cui and Bustin (2005) model among others.

Advances in the understanding of the coal properties, the storage mechanisms and the permeability system leads to an increase of the CBM production in the last few years as well as an increase in the interest in ECBM techniques. Pilot projects implementing ECBM technologies have been developed bringing as a result a better understanding of the CBM production requirements and the challenges that have to be faced. Koperna et al. (2009) and Oudinot et al. (2009) present the development and the results of a pilot  $CO_2$ -ECBM project in the Pump Canyon, San Juan Basin. The objective of this pilot project was to evaluate the effectiveness of  $CO_2$  storage in a coalbed.  $CO_2$  was injected into the coalbed for a one year period and different techniques like time-lapse seismic and evaluation of the surface

deformation were used to monitor the movement of the CO<sub>2</sub> flood. As a result of this project, after injection there was no leakage of CO<sub>2</sub> to the surface. Clarkson and Bustin (2010) present a review of the techniques available for coal reservoir characterization and summarize the challenges that can be found during CBM and ECBM production.

As advances in ECBM techniques are achieved, it is also important to pay attention to the development and improvement of monitoring techniques that can be used during and after gas injection. McCrank and Lawton (2009), present the results of the interpretation of seismic data that was acquired to monitor a CO<sub>2</sub> flood injected in the Ardley coals, Alberta, Canada. An impedance anomaly was associated to the CO<sub>2</sub> plume in the coalbed and a Gassmann fluid substitution was performed in order to model the decrease in elastic impedance. Zarantonello et al. (2010) developed a work flow to generate a seismic model associated with the storage of CO<sub>2</sub> in coalbeds. In this work geological, petrophysical, and reservoir data are integrated to produce a 3D time-lapse seismic simulation during CO<sub>2</sub>-ECBM. Lespinasse and Ferguson (2011) and Lespinasse et al. (2012), evaluate time-lapse seismic and Elastic Impedance as monitoring tools for primary and enhanced production of CBM using datasets from the Mannville coals and the Fruitland coals respectively.

### **1.5 Thesis objectives**

The objective of this project is to evaluate time-lapse seismic and attributes like Elastic Impedance (EI) and Elastic Impedance Coefficient (EC) as monitoring tools during primary and CO<sub>2</sub>-ECBM production. In order to achieve this goal, this project was divided in two parts: 1) the use of seismic as a monitoring tool during primary production and 2) the estimation of EI and EC to monitor CO<sub>2</sub> injected in a coalbed during CO<sub>2</sub>-ECBM.

In the first part of this thesis, a data set from the Mannville Coals in the Corbett Field area is used to model the seismic response of coalbeds during primary production having the following specific objectives:

- Study changes in the seismic response caused by the variation of the fluid saturation in the pore space
- Evaluate the amplitude versus offset response produced by coalbeds during primary production
- Determine seismic resolution limits by modelling different coal thicknesses

For the second part of this thesis, looking for a more complete data set, coal data from the Fruitland Formation in the San Juan Basin is used to estimate EI and EC attributes over a coalbed during CO<sub>2</sub>-ECBM production. This is done to:

- Attempt to discriminate coals saturated with methane from coals saturated with CO<sub>2</sub>
- Evaluate the possibility of monitoring the movement of the CO<sub>2</sub> flood by using this attributes
- Compare the results obtained with both attributes

## **1.6 Thesis outline**

Based on a workflow previously developed by Zarantonello et al. (2010) to generate a 3D seismic model and monitor CO<sub>2</sub> storage in a coalbed, this thesis presents the evaluation of two techniques as monitoring tools during primary and CO<sub>2</sub>-ECBM production: time-lapse seismic and estimation of the EI and EC seismic attributes.

Chapter 2 of this thesis presents an introduction to the concepts that support the development of this thesis. This chapter includes a description of the fundamentals of CBM reservoirs and CBM primary and enhanced production techniques. The details of the

Palmer and Mansoori (1998) permeability model and the Gassmann fluid substitution, which represent an important part of the methodology applied in this project, are also presented in this chapter.

Chapter 3 shows the evaluation of the time-lapse seismic during primary production. For the development of this chapter, a data set from the Mannville coals in the Corbett Creek Field, Alberta, is used. This chapter includes a complete description of the area of study and a detailed explanation of each one of the steps followed in the methodology. At the end of this chapter the results are discussed and a brief summary is included.

Chapter 4 constitutes the application of a similar methodology to the one applied in chapter 3, to data set from the Fruitland Formation, in the San Juan Basin, US, in order to perform an Elastic Impedance analysis for CO<sub>2</sub> monitoring in coalbeds. The obtained results are presented in the last part of the chapter followed by a summary of the chapter.

Finally, Chapter 5 is dedicated to the conclusions of the thesis. The conclusions are divided in two sections: the first one corresponds to the results obtained for the time-lapse seismic as a monitoring tool and the second one corresponds to the evaluation of the seismic attributes EI and EC to monitor the movement of a CO<sub>2</sub> plume during CO<sub>2</sub>-ECBM operations.

## **Chapter 2. Theoretical development**

### **2.1 Coalbed Methane (CBM)**

Coalbed Methane (CBM) is considered an unconventional resource in which the coalbed acts as a source and as a reservoir rock (McCrank and Lawton, 2009). Methane in coalbeds is originated as consequence of bacterial and geochemical processes suffered by the organic matter over the burial period (Jenkins et al., 2008).

An important characteristic of coalbeds is that they have three porosity systems classified according to their size: the micropores, the mesopores, and the macropores. The micropores are less than 2 nm, and the mesopores are in the range of 2-50 nm (De Silva et al., 2012). They correspond to the coal matrix porosity (Lin et al., 2008) and control the gas accumulation into the coal. The cleats, natural fractures formed during the coalification process, constitute the macroporosity system (Clarkson and Bustin, 2010) presenting a width that varies from millimetres to centimeters. They are divided into two categories: the face cleats, characterized by being continuous along the coalbed; and the butt cleats that are discontinuous and end against the face cleats (Figure 1) (Shi and Durucan, 2005). The cleats are responsible for the storage of the free gas existing in coals (Lin et al., 2008) and are thought as the ones that determine the coalbeds' permeability (Clarkson and Bustin, 2010).

Methane can be found in coalbeds as a free gas in the porous space, adsorbed in its structure (micropores in the coal matrix), and dissolved in water present in the cleats (De Silva et al., 2012). The CBM present in the pore space, as a free gas, represents 10% of the CBM and is normally accompanied by gases like N<sub>2</sub> and CO<sub>2</sub>. The other 90% of the

CBM is adsorbed into its matrix due to the effect of the Van der Waal forces (Peng et al., 2006).

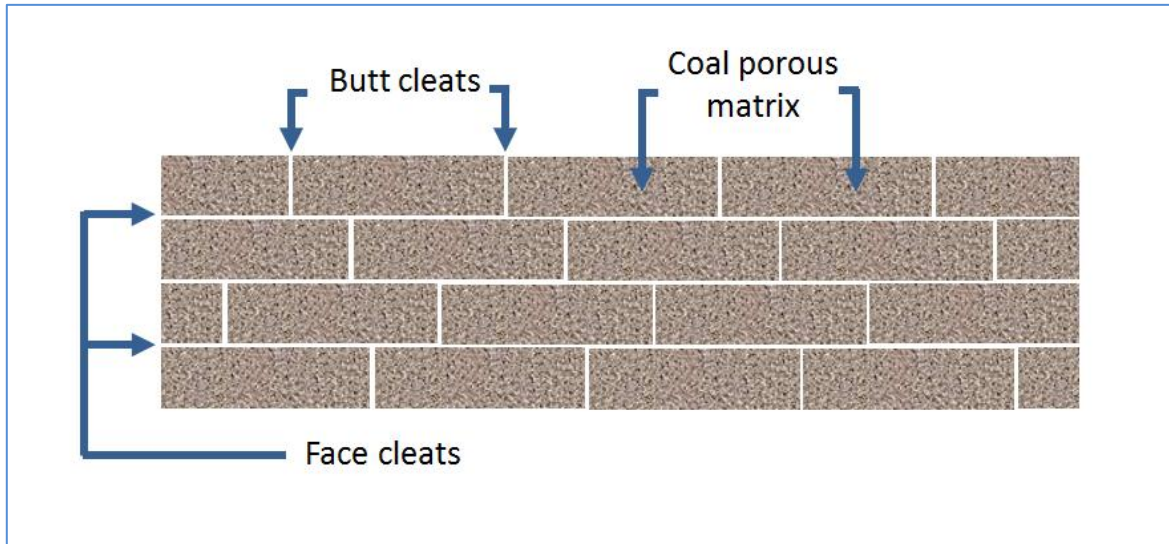


**Figure 1. Cleat system in coalbeds.**

The movement of the fluids in coalbeds occurs at two levels: diffusion of the gas in the coal matrix, and fluid flow through the cleats. The movement of fluid through the cleats is governed by the reservoir pressure and can be described using Darcy's law while the slow diffusion of gas into the coal matrix is controlled by the gas concentration (Busch and Gensterblum, 2011). Since the diffusive movement of fluids in the coal matrix is slower than the convective fluid flow that occurs in the cleats, CBM reservoirs are considered fractured reservoirs in terms of fluid flow (Robertson and Christiansen, 2008).

### ***2.1.1 CBM production***

CBM production started in the 1970's when the Department of Energy (DOE) and the United States Bureau of Mines (USBM) starts an experimental program for CBM production, using technology previously developed for the conventional production of oil and gas. This program was applied to 11 locations in the United States. In the 1980's, the

Gas Research Institute created a program dedicated to the development of technology for CBM production, and most of its results are still used (Clarkson and Bustin, 2010).

The most common method of CBM production is the reduction of the reservoir pressure (McCrank and Lawton, 2009). This process involves three stages: desorption, diffusion and fluid flow according to Darcy's law. The production of CBM takes place when a reduction of the pressure at reservoir level causes desorption of methane from the coal matrix. As a consequence, the gas pressure in the porous matrix exceeds the pressure in the cleats and will start the diffusion process (from the coal matrix to the cleats). Finally, the gas starts to flow through the cleats until it reaches the wellbore (Figure 2) (Lin et al., 2008). In the presence of coalbeds with high water content, the process begins with a water production period, resulting in the pressure reduction required for the methane desorption (Clarkson and Bustin, 2010). During CBM production, it is important to consider that the composition of the gas may change during depletion since the components that have a higher affinity to coal will remain in the coal matrix (in the adsorbed state) until the pressure decrease is enough to be desorbed (Clarkson, 2003).

Conventional primary CBM production has been claimed to be inefficient since the recovery rates are around 20-60% of the total gas in place (Gorucu et al., 2007). Factors like gas saturation and composition as well as changes in reservoir pressure are important during CBM production because they can affect the porosity systems in coals and can also have an important impact on the stability of the wellbore (Deisman et al., 2009).

### ***2.1.2 Enhanced coalbed methane***

Enhanced coalbed methane (ECBM) techniques have been developed with the purpose of increasing the recovery of gas in place that can be obtained with CBM primary

production (Shi and Durucan, 2005). ECBM consist in the injection of gas into the coalbeds to improve CMB production by stimulating the methane desorption (De Silva et al., 2012). Several ECBM techniques has been suggested (Lin et al., 2008), with  $N_2$  and  $CO_2$  injection being the most relevant procedures (Shi and Durucan, 2005).

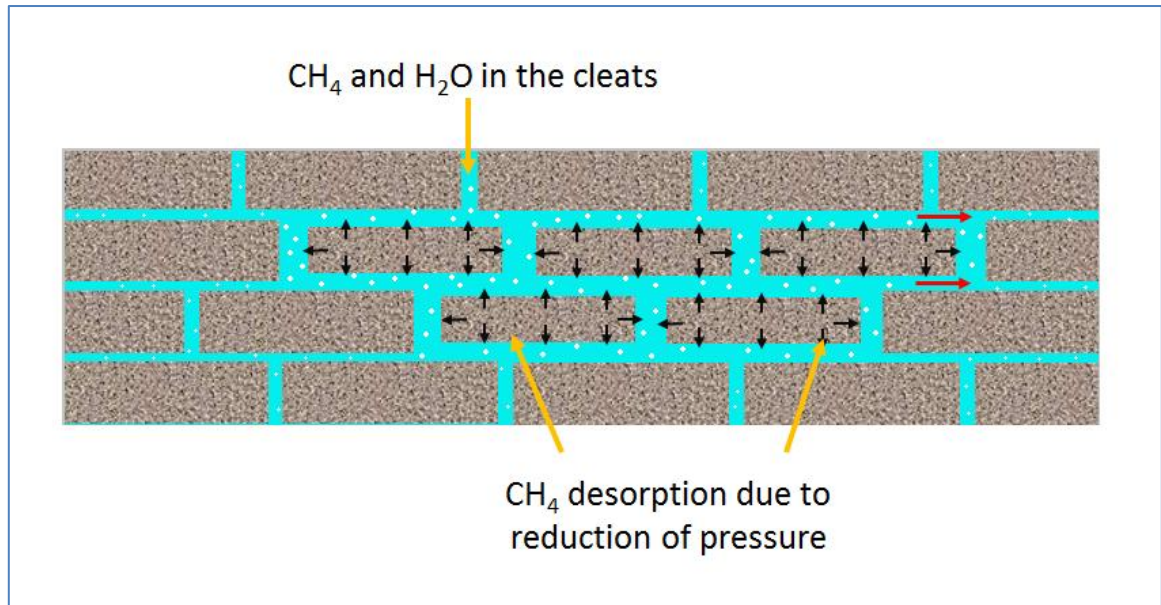


**Figure 2. Methane desorption from a coal matrix. As reservoir pressure decreases as a consequence of water production, methane desorbs from the coal matrix.**

The injection of  $N_2$  into the coalbed is a gas stripping process that enhances CBM production by generating a decrease in the partial pressure of the methane in the cleats (Mazumder and Wolf, 2008). Then, an exchange of gases, methane by  $N_2$ , occurs in order to compensate for the pressure variation, and to restore the balance into the coal (Koperna et al., 2009).

The  $CO_2$ -ECBM is based on the fact that coals have more affinity to  $CO_2$  than methane (McCrank and Lawton, 2009). The ECBM process starts when the injected  $CO_2$  moves through the cleats in the coalbed and is adsorbed by the coal matrix. During this

adsorption process, the CO<sub>2</sub> partially replaces the methane, causing an increase of the free methane concentration in the coal matrix. As a consequence, a methane diffusion process occurs from the coal matrix towards the cleats (Busch and Gensterblum, 2011). Finally, the methane in the cleats moves through the most permeable areas for production (Koperna et al., 2009). The ECBM using CO<sub>2</sub> has extra benefit in which coals can act as sites for CO<sub>2</sub> storage in the subsurface, contributing in the reduction of the emission of gases that cause the greenhouse effect (Koperna and Riestenberg, 2009). Studies have determined that coal has more predisposition to adsorb CO<sub>2</sub> than CH<sub>4</sub> and N<sub>2</sub>, being able to store big quantities of CO<sub>2</sub> (Koperna et al., 2009).

The first test of CO<sub>2</sub>-ECBM is the Allison Pilot Project and was developed in the San Juan Basin in the USA (Shi and Durucan, 2005).

An important aspect that should be considered, during the application of this technique, is that due to the interaction of the injected fluid with the coal, the coal matrix properties can suffer alterations or changes (Balan and Gumrah, 2008).

### ***2.1.3 Changes in the coal matrix due to CBM and CO<sub>2</sub>-ECBM production***

The primary and enhanced recovery of CBM generate changes in the reservoir conditions like the reservoir pressure, composition of the gas, gas sorption, and stress; bringing as a consequence important variations in the coal permeability during depletion (Gu and Chalaturnyk, 2006).

In general, the gas adsorption causes the swelling of the coal matrix while the gas desorption causes its shrinkage. The changes in the coal matrix due to gas sorption (swelling and shrinkage) are known as sorption-induced strain and results in changes of the cleat spacing and hence in coal permeability and porosity (Robertson and Christiansen,

2007). At relatively low pressures, the sorption-induced strain tends to increase, while at high pressures shows asymptotic behaviour (Robertson, 2008).

During CBM primary production, two events determine the changes in permeability suffered by the coal (Shi and Durucan, 2005). The first one is a reduction of pressure that leads to a variation in the effective stress in the coalbed. In this case the overburden pressure remains constant while the effective stress increases and causes a reduction in the cleat spacing due to compression; hence there is a decrease in permeability (Lin et al., 2008). The second one is the desorption of gases from the matrix of the coal which causes the shrinkage of the matrix. During this event, there is a decrease of the stress in the horizontal direction, and as a consequence the permeability of the coal increases (Figure 3) (Shi and Durucan, 2005). In summary, there is a reduction in the coal permeability due to the decrease in pressure during depletion, and an increase of permeability caused by the shrinkage of the matrix (Gu and Chalaturnyk, 2006).

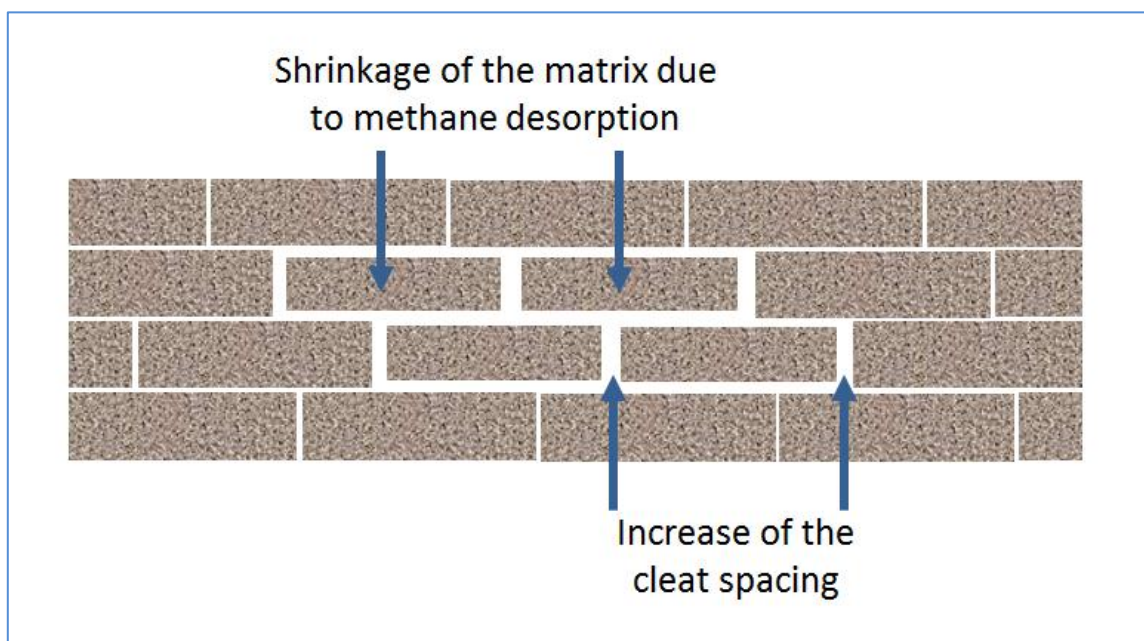


**Figure 3. Coal matrix shrinkage due to methane desorption.**

In the case of CO<sub>2</sub>-ECBM, the coal permeability decreases due to a differential swelling caused by CO<sub>2</sub> adsorption and methane desorption. As mentioned before, the methane desorption causes shrinkage of the matrix while CO<sub>2</sub> adsorption will cause a swelling effect (Chen et al., 2009). Since coal preferentially adsorbs CO<sub>2</sub> over methane and is able to store more CO<sub>2</sub> than methane (Chen et al., 2009), the swelling of the coal matrix due to CO<sub>2</sub> desorption will overcome the matrix shrinkage effect caused by gas desorption, leading to a decrease in permeability and porosity. The permeability reduction also causes a decrease in the CO<sub>2</sub> injection and CBM production rate (Chen et al., 2009).

## 2.2 Coal permeability modelling

### 2.2.1 Langmuir Isotherm

In coalbeds, the gas is present in the cleats and is also adsorbed in the coal matrix (Peng et al., 2006). The gas adsorption and desorption in coalbeds can be modeled with the Langmuir isotherm equation (Shi and Durucan, 2005) which allow the estimation of the quantity of gas that is adsorbed into the coal matrix in terms of pressure (Mitra and Harpalani, 2007). The Langmuir model is based on the theory that a surface contains a finite quantity of adsorption locations and that each location can take only one gas molecule. Therefore, the Langmuir isotherm can describe the portion of locations that are taken according to the pressure (Vandamme et al., 2010). The Langmuir isotherm is represented by the following equation:

$$V = V_L \frac{P}{P_L + P}, \quad (1)$$

where  $V$  is the adsorbed volume of gas;  $V_L$  is called the Langmuir Volume or capacity of adsorption, and is equivalent to the maximum volume of gas that is adsorbed when pressure

tends to infinite;  $P_L$  is the pressure at which the adsorbed gas volume  $V$  becomes half of the Langmuir Volume ( $V_L/2$ ) and is called Langmuir pressure; and  $P$  is the pore pressure (Robertson, 2008). This relationship establishes that the permeability of the cleats does not change linearly with the reduction of the pressure (Shi and Durucan, 2005).

The Langmuir isotherm model also assumes that:

- Adsorption takes place on a homogeneous surface in which the energy of adsorption is the same at each point (Pan and Connell, 2009)
- The adsorbed molecules do not interact between each other. This condition also applies to the adsorption locations
- The surface can adsorb only one layer of molecules (Bell and Rakop, 1986)

The Langmuir model predicts the gas adsorption of systems with only one gas component. In the case of a system with a gas mixture, i.e. two or more components, it is necessary to use the Extended Langmuir model (Chen et al., 2009). The Extended Langmuir model requires data from the adsorption isotherm of the single components (Clarkson, 2003) and is defined according to:

$$V_i = \frac{(V_L)_i P_i}{(P_L)_i + \sum_j \frac{P_j}{(P_L)_j}}, \quad (2)$$

where  $V_i$  is the adsorbed volume of the  $i$  component,  $P_L$  and  $V_L$  are the Langmuir Pressure and Langmuir volume from the single component Langmuir isotherm, and  $P_i$  and  $P_j$  are the partial pressures of the components  $i$  and  $j$  (Mitra and Harpalani, 2007).

This model is most frequently used for the estimation of the adsorption of a mixture of gas in coalbeds (Mitra and Harpalani, 2007), more specifically the displacement of methane by CO<sub>2</sub> (Chen et al., 2009).

### 2.2.2 *Palmer and Mansoori permeability model*

During production in coalbed reservoirs, two factors influence the changes in permeability. The first one is the compression of the cleats due to an increase of the effective stress that lead to a reduction of permeability. The second one is the matrix shrinkage generated by the methane desorption as consequence of the decrease of the reservoir pressure, causing an increase of the permeability (Palmer and Mansoori, 1998). In 1998, Palmer and Mansoori developed a permeability model for coal reservoirs.

The Palmer and Mansoori permeability model (Palmer and Mansoori, 1998) determines the variations in permeability as a consequence of the pressure decrease during reservoir depletion and the shrinkage of the matrix caused by methane desorption (Palmer, 2009). The Palmer and Mansoori model (Palmer and Mansoori, 1998) is defined by the following equations:

$$\frac{\phi}{\phi_i} = 1 + \frac{C_f}{\phi_i}(P - P_i) + \frac{\varepsilon_\infty}{\phi_i} \left( \frac{K}{M} - 1 \right) \left( \frac{P}{P + P_\varepsilon} - \frac{P_i}{P_i + P_\varepsilon} \right), \quad (3)$$

and,

$$C_f = \frac{1}{M} - \left( \frac{K}{M} + f - 1 \right) \beta, \quad (4)$$

where  $\phi$  is the cleat porosity,  $\phi_i$  is the cleat porosity at the initial reservoir pressure,  $C_f / \phi_i$  is the fracture compressibility,  $P$  is pressure,  $P_i$  is the initial reservoir pressure,  $\varepsilon_\infty$

is the volumetric strain at infinite pressure,  $P_\varepsilon$  is the pressure at a strain equal to  $0.5\varepsilon_\infty$  or Langmuir Pressure,  $K$  is the Bulk Modulus,  $M$  is the constrained axial modulus,  $\beta$  is the grain compressibility (Clarkson et al., 2010), and  $f$  is an empirical factor that corrects the grain compressibility and is usually approximate to 0.5 (Bradley and Powley, 1994). In the Palmer and Mansoori model (Palmer and Mansoori, 1998), porosity and permeability are related by equation 5:

$$\frac{k}{k_i} = \frac{\phi^3}{\phi_i^3}, \quad (5)$$

where  $k$  is the permeability and  $k_i$  is the initial permeability (Palmer and Mansoori, 1998).

### 2.3 Fluid substitution and Gassmann's equation

Fluid substitution is a technique that estimated changes in the seismic response as well as in density that occur as a consequence of variations in the fluid saturations in a reservoir (Kumar, 2006). This technique allows an evaluation of the response that should be obtained for a specific fluid or mix of fluids in the pore space, based on the real conditions of the reservoir at the moment in which the well data were measured (Dvorkin et al., 2007).

Fluid substitution is an important method that provides complementary information for well data analysis (Dvorkin et al., 2007); evaluation of amplitude versus offset (AVO) response, and development of 4D surveys (Smith et al., 2003). More than that, this tool makes possible the estimation of seismic velocities and density during the different stages of a reservoir, based on the fluid saturations (Han and Batzle, 2004).

Gassmann (1951) developed an equation for fluid substitution that relates the bulk modulus of the saturated rock to the porous space, pore fluid properties, mineral

composition, and the frame of the rock (Dvorkin et al., 2007). Equation 6 represents a general form of Gassmann equation (Gassmann, 1951).

$$K_{sat} = K^* + \frac{\left(1 - \frac{K^*}{K_0}\right)^2}{\frac{\phi}{K_{fl}} + \frac{(1-\phi)}{K_0} - \frac{K^*}{K_0^2}}, \quad (6)$$

where  $K_{sat}$  is the bulk modulus of the saturated rock,  $K^*$  is the bulk modulus of the dry rock,  $K_0$  is the bulk modulus of the mineral matrix,  $K_{fl}$  is the bulk modulus of the fluid in the pore space and  $\phi$  is the porosity (Smith et al., 2003).

During the formulation of Gassmann's equation (Gassmann, 1951), some assumptions were made. First, Gassmann (1951) assumes an isotropic medium that represents a homogeneous and monomineralic matrix. This assumption is usually violated because the majority of the rocks present a certain degree of anisotropy (Han and Batzle, 2004). Secondly, this equation assumes that the pores are connected, allowing the movement of the fluids through them (Smith et al., 2003). Finally, there are not chemical interactions between the pore fluids and the frame of the rock that can modify the frame properties of the rocks over the time (Han and Batzle, 2004). This last assumption leads to an important condition, the bulk modulus of the rock frame and the shear modulus will remain as constants during the fluid substitution process (Smith et al., 2003).

In practice, to do a fluid substitution, it is necessary to calculate the properties of the rock associated with the initial stage. The initial conditions are obtained from well log information, allowing the calculation of  $K_{sat}$  and  $K_{fl}$  as well as the shear modulus (Kumar, 2006). Using equation 6, it is now possible to determine the bulk modulus of the dry rock

(frame of the rock). After the properties of the dry rock are estimated, it is possible to calculate (using the same equation) properties of the rock saturated with a new fluid (Smith et al., 2003).

## 2.4 Elastic Impedance

Since changes in Acoustic Impedance (AI) are associated with changes observed in amplitude, the relationship has been used for the calibration of zero offset data (Connolly, 1999). The concept of Elastic Impedance (EI) comes from the need to find an analogue of AI for calibration and inversion purposes of far offset seismic data (Duffaut et al., 2000).

The EI development starts in the 1990s as a tool that was initially used for fluid evaluation during the assessment and development of the Fonaiven Field, located in the west of the Shetland Islands (Whitcombe et al., 2002), where the reservoirs from the Tertiary are characterized by being class II and III in the AVO classification (Connolly, 1999).

Connolly (1999) presents the derivation of the EI, which is based on the Aki and Richards (1980) linearization of the Zoeppritz equation (Connolly, 1999):

$$R(\theta) = A + B \sin^2 \theta + C \sin^2 \theta \tan^2 \theta, \quad (7)$$

where  $A$ ,  $B$  and  $C$  are defined according to (Connolly, 1999):

$$A = \frac{1}{2} \left( \frac{\Delta V_p}{V_p} + \frac{\Delta \rho}{\rho} \right), \quad (8)$$

$$B = \frac{\Delta V_p}{2V_p} - 4 \frac{V_s^2}{V_p^2} \frac{\Delta V_s}{V_s} - 2 \frac{V_s^2}{V_p^2} \frac{\Delta \rho}{\rho}, \quad (9)$$

$$C = \frac{1}{2} \frac{\Delta V_p}{\bar{V}_p}, \quad (10)$$

and  $\Delta V_p$ ,  $\bar{V}_p$ , and  $V_s^2 / V_p^2$  are estimated as follows (Connolly, 1999):

$$\bar{V}_p = \frac{V_p(t_i) + V_p(t_i - 1)}{2}, \quad (11)$$

$$\Delta V_p = V_p(t_i) - V_p(t_i - 1), \quad (12)$$

$$\frac{V_s^2}{V_p^2} = \frac{\frac{V_s^2(t_i)}{V_p^2(t_i)} + \frac{V_s^2(t_i - 1)}{V_p^2(t_i - 1)}}{2}. \quad (13)$$

The variables  $\Delta V_s$ ,  $\bar{V}_s$ ,  $\Delta \rho$ , and  $\bar{\rho}$  in a similar way than for  $V_p$ . Connolly (1999) also describes EI based on the AI equation for reflectivity, according to:

$$R(\theta) = \frac{EI(\theta)_{n+1} - EI(\theta)_n}{EI(\theta)_{n+1} + EI(\theta)_n}. \quad (14)$$

Based on the Aki and Richards (1980) linearization of the Zoeppritz equation and equation 14, Connolly (1999) approximates EI to:

$$EI = V_p^{(1+\tan^2 \theta)} V_s^{(-8K \sin^2 \theta)} \rho^{(1-4K \sin^2 \theta)}, \quad (15)$$

as a function that relates the compressional wave velocity ( $V_p$ ), the shear wave velocity ( $V_s$ ), the density ( $\rho$ ) and the angle of incidence ( $\theta$ ) (Connolly, 1999). In this equation,  $K$  is considered a constant in the area of interest and is estimated as the mean value of  $(V_s / V_p)^2$  of the section of interest in the well logs.

Using equation 16 it is possible to define  $R(\theta)$  in terms of  $R_{pp}(\theta)$ ,  $R_{ss}(\theta)$  and  $R_{\rho\rho}(\theta)$  as is shown in equation 17.

$$\Delta \ln(EI) = (1 + \tan^2 \theta) \Delta \ln(V_p) - (8K \sin^2 \theta) \Delta \ln(V_s) + (1 - 4K \sin^2 \theta) \Delta \ln(\rho) \quad (16)$$

$$R(\theta) = (1 + \tan^2 \theta) R_{pp}(\theta) - (8K \sin^2 \theta) R_{ss}(\theta) + (1 - 4K \sin^2 \theta) R_{\rho\rho}(\theta) \quad (17)$$

The main application of EI is as a tool to perform calibration of far offset seismic data. In this order, synthetic seismograms in terms of the incidence angle can be generated for calibration or inversion of non-zero offset seismic. Connolly (1999) shows examples of the use of EI logs for well tie and far-offset seismic inversion (Connolly, 1999).

Another important application of the EI consist in its use to perform a preliminary evaluation of the amplitude versus offset (AVO) response in an efficient and time effective way. Also, the changes in Elastic Impedance can be evaluated to determine a correlation with any rock property that allows us to achieve; for example, lithology or fluid discrimination (Connolly, 1999).

In 2008, Cao et al. introduced the concept of the Elastic Impedance Coefficient (EC) as a relationship proportional to the Elastic Impedance and inversely proportional to Acoustic Impedance (equation 18).

$$EC = \frac{EI}{AI}. \quad (18)$$

The EC establishes a combination of the AI and EI to create a stronger attribute for lithology, and fluid discrimination; and gas saturation estimation. Cao et al. (2008), provide some examples in which the EC produced better results for lithology discrimination and the detection of the presence of gas than the EI and the AI by themselves (Cao et al., 2008).

### **Chapter 3. Evaluation of the seismic response of coalbeds. 1D analysis. Mannville coals, Corbett field, Alberta Canada**

In this chapter, I present an evaluation of the seismic response due to fluids in the pore space of coalbeds. The development of this chapter is based on the implementation of a work flow previously developed, by Zarantonello et al. (2010), to evaluate seismic as a monitoring tool for CO<sub>2</sub> storage in coals. Initially, a fluid simulation is performed in order to predict the reservoir production history, the proportions of brine and methane in the pore space during production, the variations of the reservoir pressure, and the coal matrix changes during depletion. With this information, a fluid substitution is completed assuming an initial state of 100% brine in the porous space, and a final state of 82% of brine and 18% of methane (after 8 years of production). As a final step, the synthetic seismograms are generated before and after fluid substitution.

Well log data from the Corbett Field are used to study the Mannville coals, one of the most important coalbed methane resources in the Province of Alberta, Western Canada.

#### **3.1 Area of study**

For the development of this part of the project, I use data from the Mannville Formation coals which contain 64% of the reserves of natural gas that comes from coals in Alberta (Gentiz et al., 2008). More specifically, data from the Corbett Field located in the Corbett Creek area, 145 km to the NW of Edmonton (Cockbill, 2008). The Corbett Field has an extension of approximately 558 km<sup>2</sup> and is located in the north central part of Alberta, Canada. A map showing the location of the area of study is presented in Figure 4.

In the Corbett Field, the first well was drilled during 2000, reaching two coal seams of the Upper part of the Mannville Group. The coal seams are at a depth of approximately

825 m in the NE area of the field, and become deeper to the SW where they reach a depth of approximately 1080 m (Cockbill, 2008). The first seam is known as the Main Seam and has a thickness of approximately 4 m, while the second one, or Lower Seam, is thinner and has an average thickness of 1.5-2 m. Overlying and underlying the Main and Lower seam, there are several coal seams, but they are thinner and have limited lateral extension (Gentiz et al., 2008).

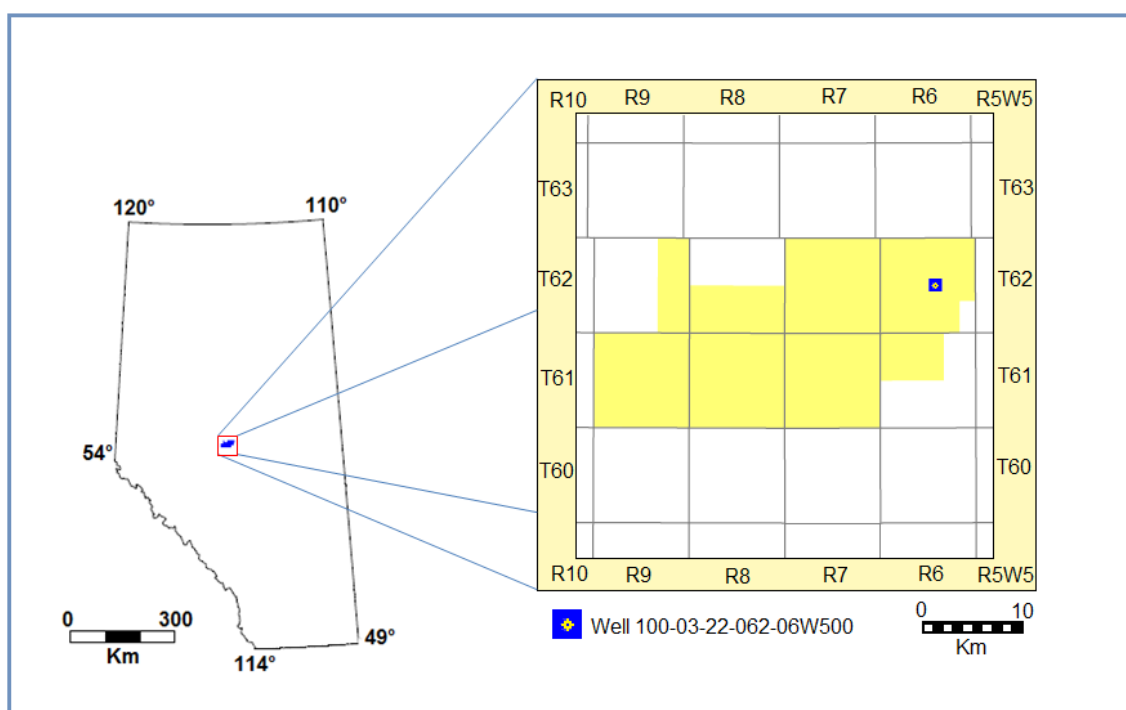


**Figure 4. Corbett Field and 100-03-22-062-06W500 well location.**

Vertical wells were drilled in the Corbett Field which result in gas production of 20-100 mcf/d. In 2004, horizontal wells were drilled in order to decrease the dewatering time and increase the gas production. The horizontal wells increase the production to 200-700 mcf/d. From 2005 to the present, multi-lateral horizontal wells have been drilled which produce an average of 2 mmcf/d of gas (Cockbill, 2008).

Well log data from the well 100-03-22-062-06W500 are used for the development of this section. Figure 4 shows the location of the well, and Figure 5 presents the well log data.

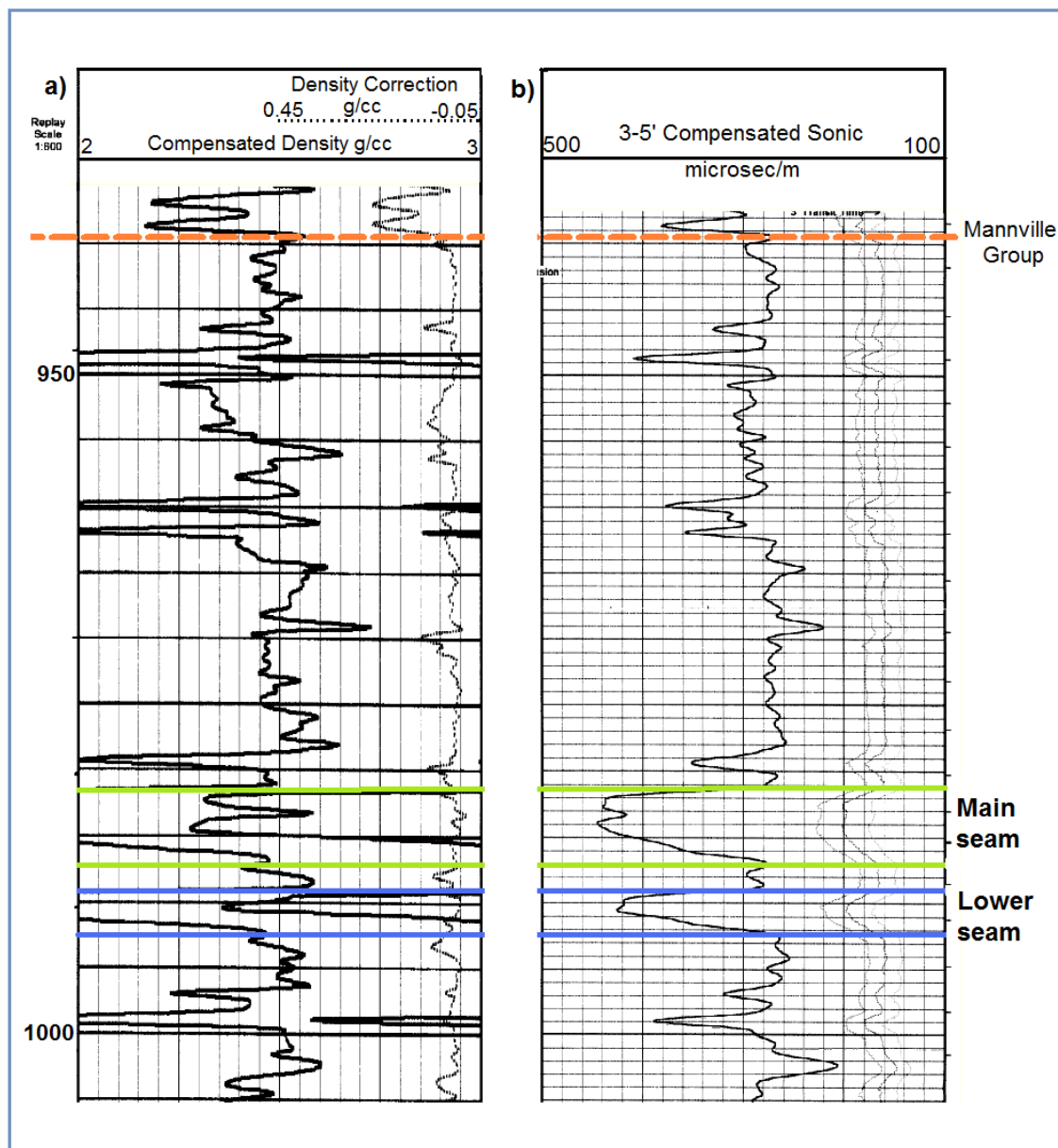


Figure 5. Well log of the well 100-03-22-062-06W500. a) Compensated density log, b) compensated sonic log.

### ***3.1.1 Mannville Group***

The Mannville Group, Ardley Coals, Horseshoe Canyon Formation and Belly River Group represent the four major coal areas in Alberta, with the Mannville Group coals being the one with the highest gas content (Beaton, 2003).

The deposition of the Mannville Group took place during the Lower Cretaceous. It extends through the southern and central Alberta Plains (Beaton, 2003). The Mannville Group is underlying the Colorado Group and overlying the pre-Cretaceous unconformity (Gentiz et al., 2008).

The base of the Mannville Group consist of sediments deposited in continental (alluvial and fluvial) and transitional (deltaic and estuarine) environments, which filled the paleotopography generated by the erosion period (Beaton et al., 2006). The Lower Mannville deposition ends with a regional transgression of the sea. (Beaton, 2003). A progradational sequence defines the middle Mannville (Banerjee and Goodarzi, 1990), with sediments from shoreline till fluvial and estuarine environments (Beaton, 2003). Finally, upper Mannville is characterized by cycles of regressive and transgressive sequences in which several coal seams were deposited (Beaton et al., 2006).

The deposition of the coals from the Upper part of the Mannville Group occurred in a fluvio-deltaic environment, and they have their origin in wood and plants that suffered a coalification process (Gentiz et al., 2008). These coal seams are known for being deep (475 m in the NE to 3600 m in the SW) (Bachu, 2007), thick, and with a low percentage of ash content (Gentiz et al., 2008).

The Upper Mannville coal rank is sub-bituminous to high volatile bituminous and has a net thickness that varies from 0.2 to 16.5 m, reaching the maximum thickness in the

west and central part of Alberta (Bachu, 2007). Red Deer represents one of the areas with the thickest net coal (6-12 m) in the Upper part of the Mannville Group, while the average net thickness is in the range of 2-6 m (Beaton et al., 2006).

In general, Mannville coal zones show temperatures higher than 31 °C and contain high salinity formation water (Bachu, 2007). Additionally, gas content is estimated on the order of 5 bcf/section for areas with a net coal thickness of approximately 4 m (Beaton et al., 2006).

### ***3.1.2 Corbett Creek coal properties***

The reflectance of the vitrinite in this area was determined by core tests and is in the range of 0.62%-0.67%. Core tests also determined the existence of bright as well as bright-dull (banded) lithotypes, and the presence of Siderite in the cleats (Gentiz et al., 2008).

The three major maceral groups are identified in Corbett Creek coals. Vitrinite is in the form of massive collotelinite while liptinite can be found in different forms including resinite, sporonite and exudanite. The third group, Inertinite, is mostly represented by the presence of telo-inertinite (Gentiz et al., 2008).

The estimated porosity for Mannville Coals in this area is 5-6% and they have a permeability of 3-4 mD. As a result of the dominant presence of vitrinite in Corbett Creek coals, there is a good formation of the cleat system, showing face cleats at an interval of 0.5 cm. The gas content has been estimated in 6-8 cm<sup>3</sup>/g, and the gas composition in these coals is mostly methane (94%) and small proportions of CO<sub>2</sub>, N<sub>2</sub> and ethane (Gentiz et al., 2008).

## 3.2 Methodology

### 3.2.1 *Data set selection and data collection*

For the development of this section, well log data from Horseshoe Canyon (Bashaw Field) and Mannville Coals (Corbett Field) are available. The two data sets are evaluated to determine the one that better fits to the goals of this part of the project.

The Horseshoe Canyon formation presents several coalbeds that can be separated in three coal zones. These are the Carbon Thompson, Daly-Weaver, and the Drumheller Coal Zone. In general, Horseshoe Canyon coals are discontinuous and the seams' thickness varies between one and two meters (Beaton et al., 2002). In addition, some Horseshoe Canyon coalbeds produce freshwater, and in some areas they have become protected zones due to the important water source that they represent (Beaton, 2003). In the case of the Bashaw Field, the well logs available show thin coal seams (1.5-2 m) at depths between 300 and 400 m.

Mannville Group coal zones are buried deeper than Horseshoe Canyon coal zones. The average net coal thickness is 2-6 m, and it has been estimated to have a high content of methane (Beaton, 2003). In the Red Deer area, the Mannville coals can reach a net thickness in the range of 6-12 m (Beaton, 2003). Another factor to consider is that the Mannville coals are wet and the salinity of the water is generally high (Finn et al., 2010). In the Corbett Creek area, well logs reveal the Mannville coals at a depth of approximately 980 m. Two coal seams can be easily identified: the Main seam of 3.65 m thickness, and a Lower seam with a thickness of 1.67 m.

The Mannville coals in the Corbett Creek area are selected for this study, based on the presence of thicker coalbeds that can generate a larger effect in the seismic response.

Once the Corbett field is selected as the area of study, data of physical properties of the Mannville coals are collected from previous published studies.

### 3.2.2 Fluid simulation

The fluid simulation is performed using data from well 100-03-22-062-06W500, assuming that the coal seam is a homogeneous medium. The fluid simulation is completed using a tank model (Figure 6) which implies that between two points there is no change in the reservoir properties, and that an average of the properties can provide a good description of the reservoir (Odeh, 1969). FAST CBM software is used to perform the fluid simulation.

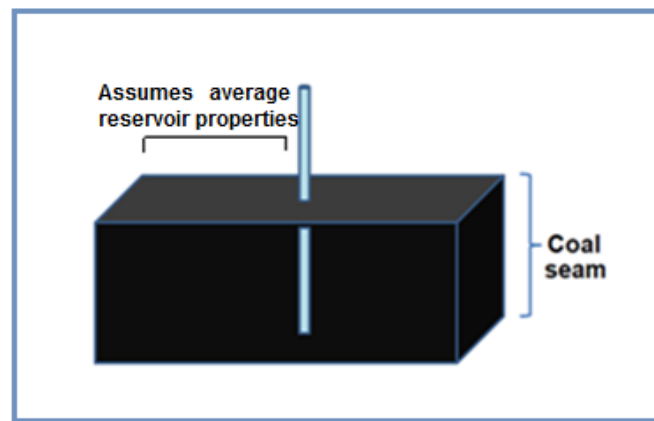


**Figure 6. Tank model assumed for fluid simulation. This model establishes that the properties of the reservoir do not vary from point to point, hence an average of the properties is used.**

Table 1 lists the parameters that describe the coal seam modelled in the fluid simulation.

The fluid simulation can be divided in three stages: construction of the Langmuir isotherm, modeling of the matrix shrinkage and deliverability, and production forecast.

**Table 1 Reservoir and pore fluid parameters**

<b>Parameter</b>	<b>Value</b>	<b>Source</b>
Reservoir temperature	40°C	Accumap
Initial reservoir pressure	9140 kPa	Accumap
Permeability	3 mD	Gentzis et al., 2008
Net thickness	5 m	Well log data. Accumap
Coal density	1.3 g/cm <sup>3</sup>	Gentzis and Bolen, 2008
Area	0.323 km <sup>2</sup>	F.A.S.T CBM default
Wellbore skin value	-2	Gentzis and Bolen, 2008
Water salinity	60000 ppm	Finn et al., 2010
Methane gravity	0.56	Batzle and Wang, 1992
Initial water saturation	100%	-----
Initial gas composition	100% CH <sub>4</sub>	-----

### 3.2.2.1 Construction of the Langmuir isotherm

At this stage of the simulation, the Langmuir parameters as well as the initial reservoir properties are required to build desorption isotherm. Table 2 shows the Langmuir parameters for methane, and Figure 7 presents the desorption isotherm build with these parameters.

**Table 2. Methane Langmuir parameters**

<b>Parameter</b>	<b>Value</b>	<b>Source</b>
Langmuir methane volume	11.76 cm <sup>3</sup> /g	Marvor and Gunter, 2006
Langmuir methane pressure	4688.43 kPa	Marvor and Gunter, 2006

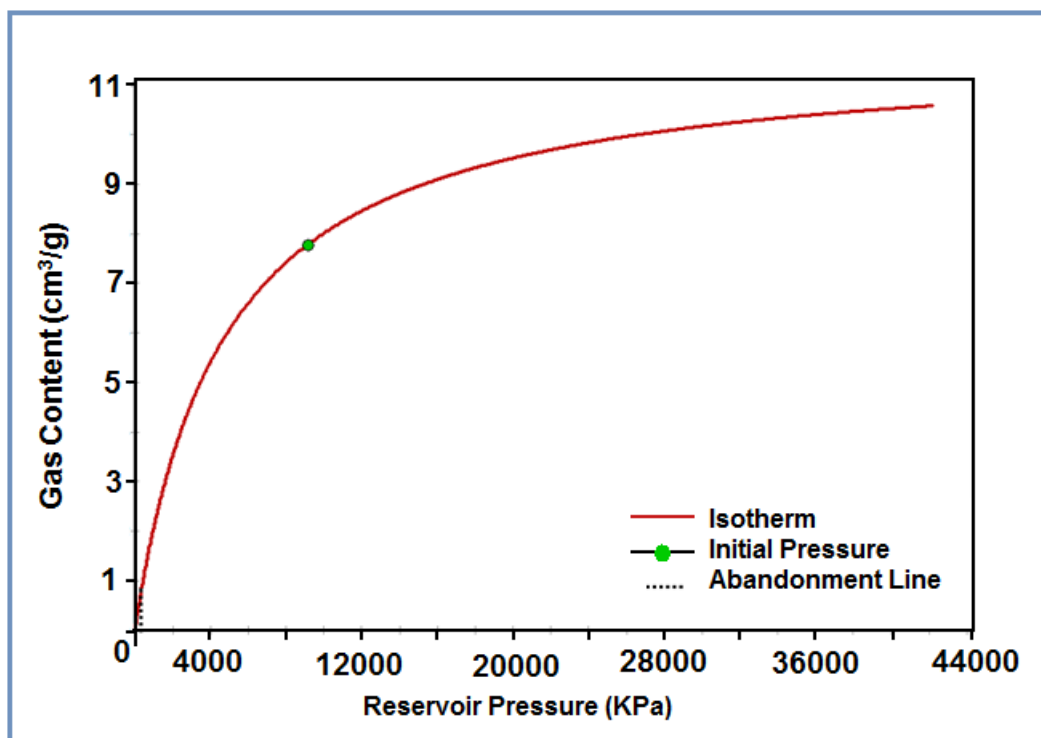


**Figure 7. Desorption isotherm. This curve determines the methane desorbed from the coal matrix at a specific reservoir pressure.**

### 3.2.2.2 Matrix shrinkage/swelling

Changes in the porosity and permeability due to swelling and shrinkage of the matrix are calculated with the Palmer and Mansoori analytical model using equation 3 (Palmer and Mansoori, 1998). The parameters required to complete this stage are presented in Table 3.

**Table 3. Parameters for the Palmer and Mansoori model.**

Parameter	Value	Source
Poisson's ratio	0.21	Marvor and Gunter, 2006
Young's modulus	2435.0 MPa	Marvor and Gunter, 2006
Bulk modulus	1399.5 MPa	Marvor and Gunter, 2006

The Palmer and Mansoori permeability model (Palmer and Mansoori, 1998) provides the variation of the porosity ratio (final porosity divided by initial porosity) in terms of pressure.

### 3.2.2.3 Deliverability and production forecast

At this stage, the relative permeability curves are included in the model. In this case, relative permeability curves of the area of study are not available. Gentzis and Bolen (2008) use the relative permeability curves of Meany and Paterson (1996) for Australian coals to do a fluid simulation for the Gates coals, the Mannville coals' equivalent in the Alberta Foothills. Based on this fact, it was decided to use the relative permeability curves presented by Meany and Paterson 1996 for the development of this part of the project. The relative permeability curves are shown in Figure 8.

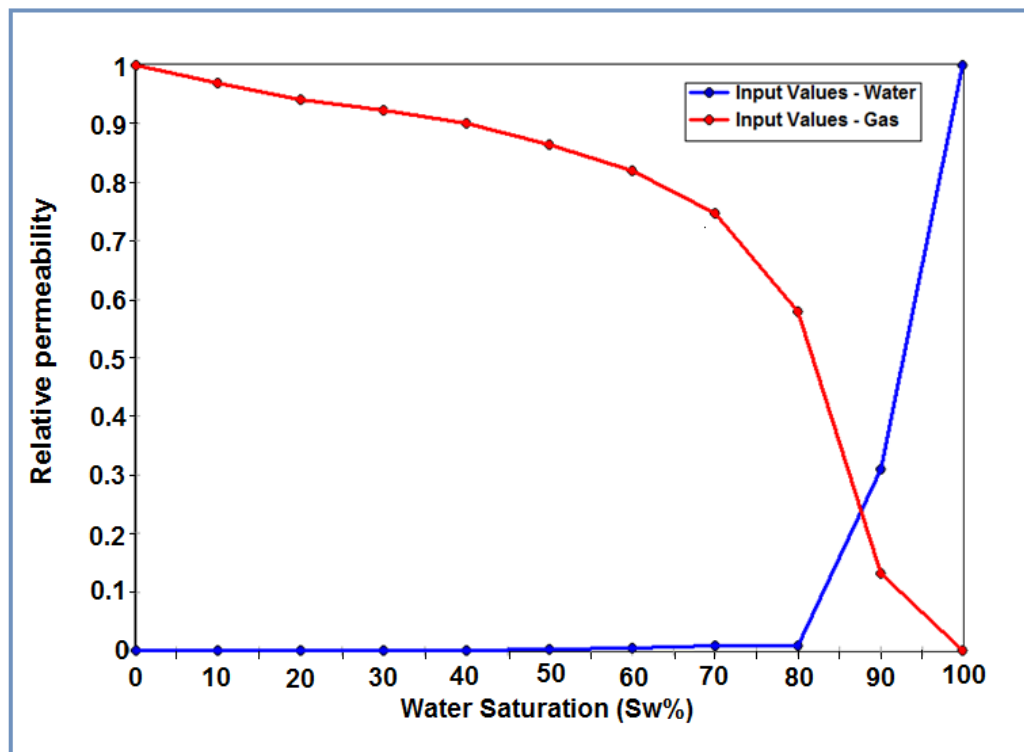


**Figure 8. Relative permeability curves.**

The production forecast provides an estimation of the reservoir behaviour during the first 10 years of production and is calculated based on desorption isotherms, the Palmer and Mansoori model (Palmer and Mansoori, 1998), and the relative permeability curves.

#### 3.2.2.4 Shear wave velocity estimation

I use the empirical relation developed by Marcote-Rios to estimate the shear wave velocity. The calculation is done according to:

$$V_s = 0.4811 V_p + 0.00382, \quad (19)$$

with the velocity in km/s. (Mavko et al., 2009).

### 3.2.3 *Fluid properties*

The fluid properties, used for the Gassmann fluid substitution, are estimated with the equations presented by Batzle and Wang (1992). They use a series of relations, based on thermodynamic laws and empirical results, to make an approximation of density, bulk modulus, velocity and viscosity of the fluids, and evaluate the dependence of these properties on the temperature, pressure, and composition of the fluids (Batzle and Wang, 1992). Below, the procedure used to calculate the gases (mixture of methane and CO<sub>2</sub>) and brine properties is presented.

#### 3.2.3.1 Gas

The specific gravity, G, defines a gas or a mixture of gases and it has values between 0.56 and 1.8. The specific gravity is calculated by dividing the density of the gas or mixture of gases by the density of the air at 1 atm and 15.6 °C. An approximation of the specific gravity of the gas will be enough to make a good estimate of its properties (Batzle and Wang, 1992).

To calculate the properties of the gas, it is necessary to estimate the pseudo-reduced temperature and pressure using the following equations:

$$P_{pr} = \frac{P}{4.892 - 0.4048G}, \quad (20)$$

$$T_{pr} = \frac{T_a}{94.72 + 170.75G}, \quad (21)$$

where  $P_{pr}$  and  $T_{pr}$  are the pseudo-reduced pressure and temperature respectively,  $P$  is the pressure (in MPa),  $G$  is specific gravity and  $T_a$  is the absolute temperature defined by equation 22 (Batzle and Wang, 1992):

$$T_a = T + 273.15, \quad (22)$$

where  $T$  is the temperature in Celsius degrees.

The density of the gas is determined using equation 23 which depends on the pressure  $P$ , specific gravity  $G$ , the compressibility factor  $Z$ , the gas constant  $R$ , and the absolute temperature  $T_a$ .

$$\rho \cong \frac{28.8GP}{ZRT_a}. \quad (23)$$

Equation 24 and 25 are used to calculate the compressibility factor  $Z$  in terms of the pseudo-reduced temperature and pressure.

$$Z = \left[ 0.03 + 0.00527(3.5 - T_{pr})^3 \right] P_{pr} + (0.642T_{pr} - 0.007T_{pr}^4 - 0.52) + E, \quad (24)$$

$$E = 0.109(3.85 - T_{pr})^2 e^{\left\{ \left[ 0.45 + 8 \left( 0.56 - \frac{1}{T_{pr}} \right)^2 \right] \frac{P_{pr}^{1.2}}{T_{pr}} \right\}}. \quad (25)$$

The bulk modulus  $K_s$  for adiabatic conditions is estimated according to:

$$K_s = \frac{P}{\left(1 - \frac{P_{pr}}{Z} \cdot \frac{\partial Z}{\partial P_{pr}}\right)_T} \gamma_0, \quad (26)$$

where the derivative  $\partial Z / \partial P_{pr}$  is calculated from equations 24 and 25, and  $\gamma_0$  with equation 27:

$$\gamma_0 = 0.85 + \frac{5.6}{(P_{pr} + 2)} + \frac{27.1}{(P_{pr} + 3.5)^2} - 8.7e^{[-0.65(P_{pr}+1)]}. \quad (27)$$

These equations are good approximations for the conditions that are usually found in exploration (Batzle and Wang, 1992).

### 3.2.3.2 Brine

Using empirical data, a relationship to estimate the density of sodium chloride solutions is developed. This relationship establishes a dependence of the density on the pressure and temperature conditions, as well as on the salinity, as follows

$$\rho_w = 1 + 1 \cdot 10^{-6} (80T - 3.3T^2 + 0.00175T^{3+B}), \quad (28)$$

$$B = 489P - 2TP + 0.016T^2P - 1.3 \cdot 10^{-5} T^3P - 0.333P^2 - 0.002TP^2, \quad (29)$$

$$\rho_B = \rho_w + S \{0.668 + .044S + 1 \cdot 10^{-6} C\}, \quad (30)$$

$$C = 300P - 2400PS + T(80 + 3T - 3300S - 13P + 47PS), \quad (31)$$

where  $\rho_w$  is the water density,  $\rho_B$  is the brine density and  $S$ , is the salinity in ppm.

Equations 30 and 31 are adequate only for sodium chloride solutions (Batzle and Wang, 1992).

The estimation of the water velocity,  $V_w$ , was calculated using equation 32 which can be used for pressure and temperature conditions up to 100 MPa and 100 °C respectively.

$$V_w = \sum_{i=0}^4 \sum_{j=0}^3 w_{ij} T^i P^j, \quad (32)$$

where  $w_{ij}$  are the constants provided in Table 4.

**Table 4. Constants for the water velocity calculation (Batzle and Wang, 1992)**

Coefficient	Value	Coefficient	Value
w <sub>00</sub>	1402.85	w <sub>02</sub>	3.437x10 <sup>-3</sup>
w <sub>10</sub>	4.871	w <sub>12</sub>	1.739x10 <sup>-4</sup>
w <sub>20</sub>	-0.04783	w <sub>22</sub>	-2.135x10 <sup>-6</sup>
w <sub>30</sub>	1.487x10 <sup>-4</sup>	w <sub>32</sub>	-1.455x10 <sup>-8</sup>
w <sub>40</sub>	-2.197x10 <sup>-7</sup>	w <sub>42</sub>	5.230x10 <sup>-11</sup>
w <sub>01</sub>	1.524	w <sub>03</sub>	-1.197x10 <sup>-5</sup>
w <sub>11</sub>	-0.0111	w <sub>13</sub>	-1.628x10 <sup>-6</sup>
w <sub>21</sub>	2.747x10 <sup>-4</sup>	w <sub>23</sub>	1.237x10 <sup>-8</sup>
w <sub>31</sub>	-6.503x10 <sup>-7</sup>	w <sub>33</sub>	1.327x10 <sup>-10</sup>
w <sub>41</sub>	7.987x10 <sup>-10</sup>	w <sub>43</sub>	-4.614x10 <sup>-13</sup>

In order to calculate the velocity of the brine,  $V_b$ , the salinity effect is included in equation 33 (Batzle and Wang, 1992).

$$V_b = V_w + SD + S^{1.5} (780 + 10P + 0.16P^2) - 820S^2, \quad (33)$$

$$D = (1170 - 9.6T + 0.55T^2 - 8.5 \cdot 10^{-5}T^3 + 2.6P - 0.0029TP - 0.0476P^2). \quad (34)$$

Table 5 present the data used in this study for the calculation of the fluid properties.

**Table 5. Data used for gas properties calculation**

<b>Property</b>	<b>Value</b>
Methane specific gravity	0.5537
CO <sub>2</sub> specific gravity	1.5189
Reservoir temperature	41.66 °C
Salinity	8000 ppm

Table 6 presents the fluid properties that are calculated with Batzle and Wang (1992) equations (equations 20 to 34 here).

**Table 6. Fluid properties at reservoir conditions.**

<b>Fluid property</b>	<b>Value</b>
<b>Liquid phase:</b>	
Brine density	1.034 g/cm <sup>3</sup>
Brine bulk modulus	2658.68 MPa
<b>Gas phase:</b>	
Methane density	0.022 g/cm <sup>3</sup>
Methane bulk modulus	5.397 MPa

#### **3.2.4 Gassmann fluid substitution**

The fluid substitution is performed by following the steps provided by Smith et al. (2003) and Kumar (2006) in their tutorials for the application of the Gassmann equation (Gassmann, 1951). The fluid substitution can be performed as a two phase process. In phase I, the initial properties of the rock are determined; this includes the initial bulk modulus and density of the saturated rock, and the estimation of the properties of the fluids

that are initially in the pore space. In phase II, the properties of the rock assuming the presence of a new mix of fluids in the pore space is estimated.

For the first phase, I assume a saturation of 100% brine in the pore space, and use the sonic and density logs of the well 100-03-22-062-06W500 (Figure 5) to determine the initial properties of the rock. The bulk modulus of the saturated rock is calculated according to:

$$K = \rho_b \left( V_p^2 - \frac{4}{3} V_s^2 \right), \quad (35)$$

where  $\rho_b$  corresponds to the bulk density taken from the density log,  $V_p$  is the velocity of the compressional wave obtained from the sonic log, and  $V_s$  is the estimated shear wave velocity (Kumar, 2006), that in this case is estimated using the Marcote-Rios relation. The shear modulus,  $\mu$ , which remains constant during the fluid substitution process, is calculated according to: (Smith et al., 2003).

$$\mu = \rho_b V_s^2. \quad (36)$$

For the bulk modulus of the mineral matrix  $K_0$ , a monomineralic matrix composed of carbon is considered in this case.

In addition, it is necessary to calculate the bulk modulus of the frame of the rock,  $K^*$ , (dry rock) according to:

$$K^* = \frac{K_{sat} \left( \frac{\phi K_0}{K_{fl}} + 1 + \phi \right) - K_0}{\frac{\phi K_0}{K_{fl}} + \frac{K_{sat}}{K_0} - 1 - \phi}, \quad (37)$$

where  $K_{sat}$  is the bulk modulus of the saturated rock,  $K_0$  is the bulk modulus of the mineral matrix,  $K_{fl}$  is the bulk modulus of the fluid in the pore space, and  $\phi$  is the fractional porosity (Smith et al., 2003).

The second phase of the fluid substitution begins with the estimation of the properties of the new fluid or desired fluid in the porous space,  $\rho_{flmix}$ . The properties of the new fluid are calculated according to the reservoir conditions after 8 years of production, taking into account the variation in pressure and changes in porosity. The fluid saturations associated with this production stage are 82% of brine and 18% of methane. The density of this mix of fluids is calculated according to:

$$\rho_{flmix} = \phi_{CH_4} \rho_{CH_4} + \phi_{brine} \rho_{brine} , \quad (38)$$

where  $\rho_{CH_4}$  and  $\rho_{brine}$  are the methane and brine density respectively, and  $\phi_{CH_4}$  and  $\phi_{brine}$  are the volumetric fraction of each component (Batzle and Wang, 1992). The bulk modulus for this mix of fluids is calculated according to:

$$\frac{1}{K_{flnew}} = \frac{\phi_{CH_4}}{K_{CH_4}} + \frac{\phi_{brine}}{K_{brine}} , \quad (39)$$

where  $K_{CH_4}$  and  $K_{brine}$  are the bulk modulus of the methane and brine (Batzle and Wang, 1992) previously calculated with the CREWES Fluid Properties Explorer application (CREWES.org).

Once the properties of the rock and pore fluid, for the initial condition, and the properties of the new mix of fluids are calculated, it is possible to determine the bulk modulus of the rock saturated with the new fluid using equation 6 (Smith et al., 2003).

The new bulk density of the rock,  $\rho_{bnew}$ , after the fluid substitution, is calculated according to:

$$\rho_{bnew} = \rho_g (1 - \phi) + \rho_{fmix} , \quad (40)$$

where  $\rho_g$  is the matrix density (Smith et al., 2003). Finally,  $v_p$  and  $v_s$  are estimated with equations 35 and 36, using the bulk modulus of the rock saturated with the new fluid (Smith et al., 2003).

The applicability of the Gassmann equation is based on assumptions about the structure and pore space of the rock. The Gassmann equation is used in coals, based on the fact that the porous matrix has low permeability and the macroporosity system (cleats) is the one that controls the fluid flow. For this study, it is assumed that the fluid substitution is performed taking into account only effective porosity.

### 3.2.5 *Synthetic seismograms*

The synthetic seismograms are generated in the depth domain, using the CREWES software SYNGRAM (CREWES.org). In order to identify the effect of the replacement of brine by methane, synthetic seismograms before and after fluid substitution are generated.

The synthetic seismograms are generated using a 30 Hz and a 60 Hz zero phase Ricker wavelet (Figure 9), and three cases are studied to evaluate the resolution limits of the seismic response: Corbett Field case (Main seam of 3.65 m and Lower seam of 1.67 m), a coal seam of 10.64 m of thickness, and a 21.28 m coal seam.

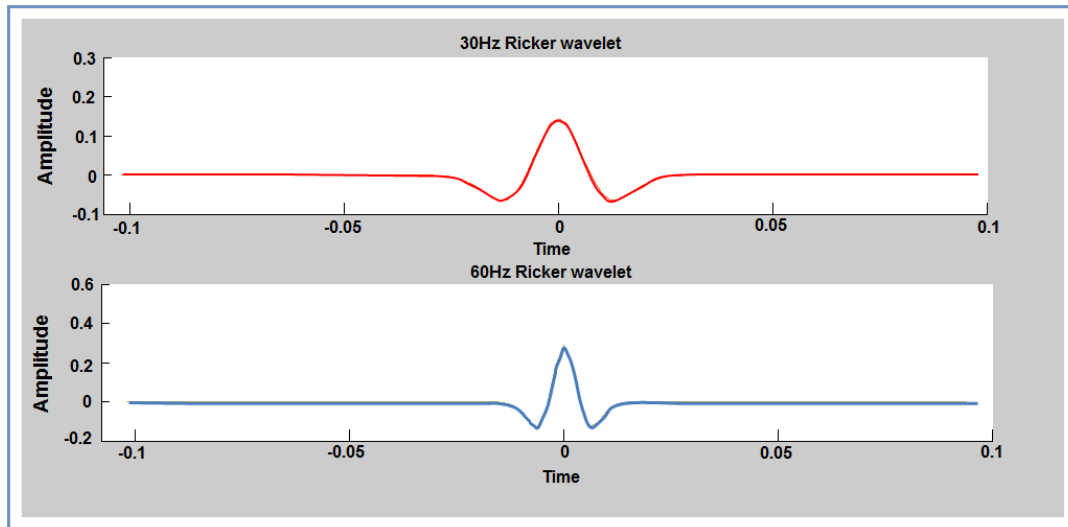


**Figure 9. 30 Hz and 60 Hz Ricker wavelets for synthetic seismograms.**

### 3.3 Results

#### 3.3.1 Fluid simulation

The fluid simulation provides information about the changes that occur in the coal matrix during methane production and an estimation of gas and water production rates in a 10 year period.

The changes in the coal matrix are estimated in terms of the porosity ratio  $\phi / \phi_i$ , where  $\phi$  is the cleat porosity and  $\phi_i$  is the cleat porosity at initial reservoir pressure, using the Palmer and Mansoori Model.

Figure 10 presents the variation of the porosity ratio with the reservoir pressure. This graph shows a decrease in the porosity ratio as the reservoir pressure decrease from 9000 kPa to 3500 kPa. In the case of primary production, which is the case studied in this section, the behaviour of the curve, in this range of pressure, can be described as consequence of an increase in effective stress. The change in the effective stress occur when reservoir pressure decrease during depletion while the stress due to the overburden

remains constant (Shi and Durucan, 2005). This leads to the decrease in the permeability/porosity as a result of the compression suffered by cleats which is evident in this segment of the curve.

At pressures lower than 3500 kPa there is a change in the curve's behaviour (Figure 10), showing an increment of the porosity ratio. The decrease of the reservoirs pressure due to depletion also causes methane's desorption and as a consequence the shrinkage of the coal matrix. This process represents an increase in the permeability/porosity (Palmer and Mansoori, 1998). At pressure below 3500 kPa the effect of the shrinkage of the coal matrix in the porosity overcomes the effect caused by the augmentation of the effective stress.

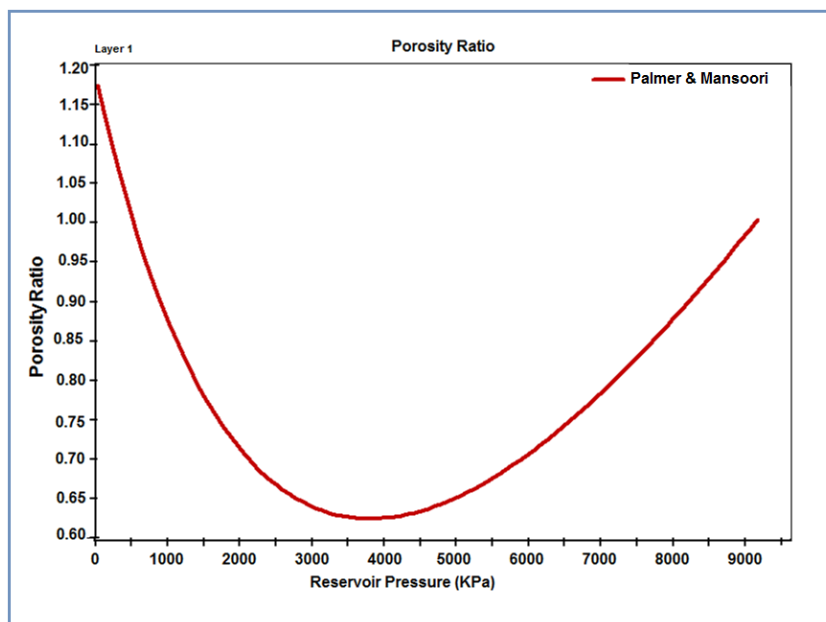


**Figure 10. Variation of the porosity ratio with the reservoir pressure, estimated with model due to Palmer and Mansoori (1998).**

Figure 11 presents the gas and water production forecast. In the water forecast curve (blue line in Figure 11), there is a rapid decrease in the water production rate during 2010

and the beginning of 2011, and it corresponds to the dewatering period. After 2011, the water production rate slowly decreases over the years. The gas production rate (red line in Figure 11) rapidly increase until it reaches its maximum point at 7500 m<sup>3</sup>/d. Then, the gas production rate start to decrease until it stabilizes approximately 4 years after the first day of production.

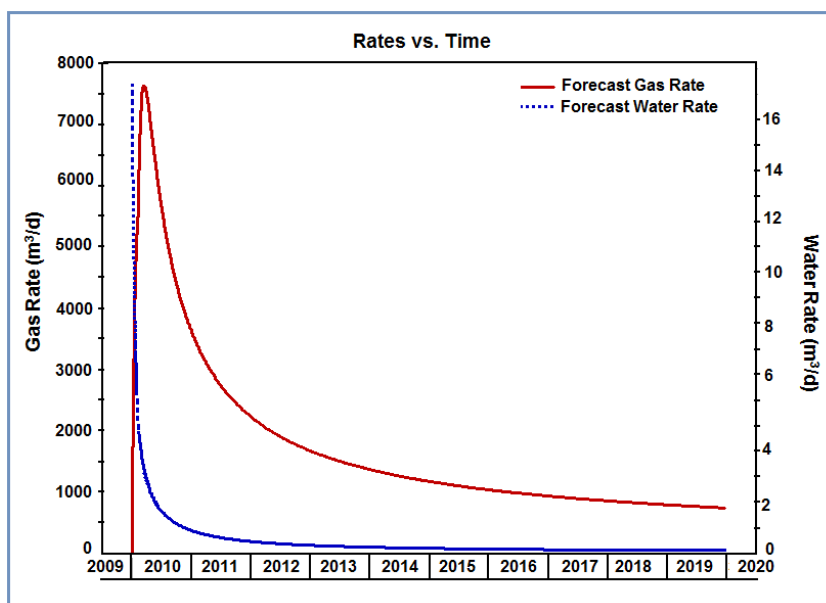


**Figure 11. Gas and water production forecast. This graph provides an estimation of the gas and water production per day along a 10 years period, starting the first day of production.**

Table 7 presents the variation of the water saturation during reservoir depletion along a 9 year period. This table present the progressive decrease of the water saturation and the increase of the presence of methane.

The results of the fluid simulation allow the estimation of the changes in porosity and the estimation of water and gas saturation after 8 years of production, providing a complete scenario for fluid substitution.

**Table 7. Water saturation variation with pressure**

<b>Date</b>	<b>Pressure (kPa)</b>	<b>Water Saturation %</b>
01/01/2010	8931.01	90.85
01/01/2011	6457.335	85.096
01/01/2012	5526.985	84.114
01/01/2013	4964.689	83.511
01/01/2014	4563.482	83.084
01/01/2015	4251.019	82.756
01/01/2016	3995.132	82.495
01/01/2017	3777.956	82.278
01/01/2018	3590.289	82.096
01/01/2019	3424.807	81.939

### **3.3.2 Synthetic seismograms**

The synthetic seismograms give an idea of the character of the seismic response of the coalbeds saturated with 100% brine and saturated with a mix of brine and methane (82% brine, 18% of methane).

#### **3.3.2.1 Case I: Corbett Field**

As it occurs in Corbett Field (Figure 5), this case evaluates the seismic response of two coal seams: the Main seam of 3.65 m and the Lower seam with a thickness of 1.67 m. Figure 12, presents the synthetic seismograms associated to the Corbett Field case, before and after fluid substitution, using a 30 Hz zero phase Ricker wavelet. In Figure 12, the synthetic seismograms present a negative reflection at a depth of approximately 980 m. This trough corresponds to the top of the Main seam as it can be correlated with the logs. At a depth of approximately 1000 m it is possible to appreciate a positive reflection which

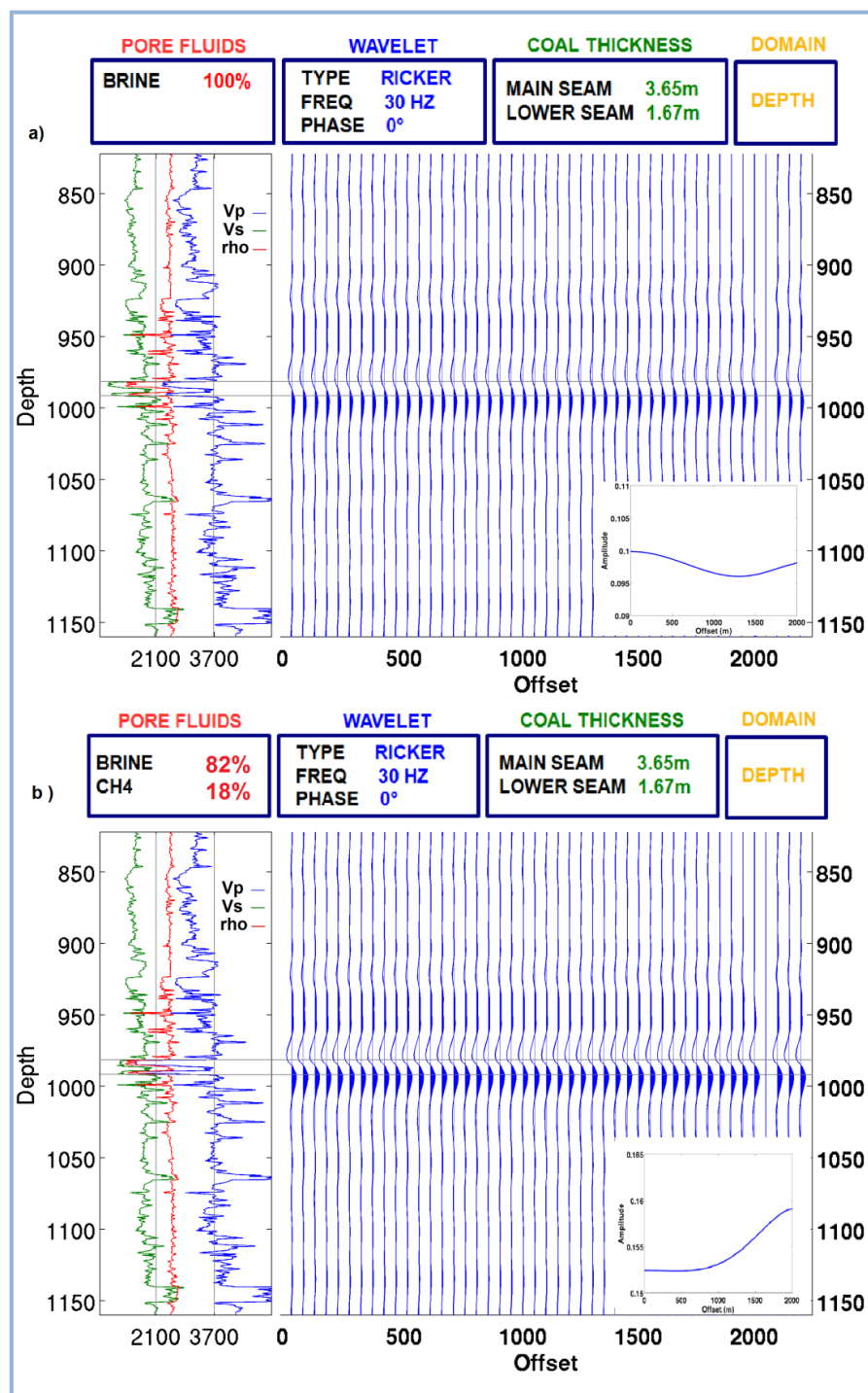
can be associated with the response of a thin coal seam (below the Lower seam) located at around 1000 m. In this case, the Main Seam, the Lower seam and the coal seam at a depth of 1000 m are being resolved as a complete unit or block.

Figure 12a represents the synthetic seismogram for the coalbeds saturated with 100% brine. The reflections associated to the top and base of the three coalbeds are weak and there is no evident AVO response.

Figure 12b presents the seismogram for the coalbeds saturated with a mix of 82% brine and 18% methane. After the fluid substitution, it is possible to appreciate an increase in the amplitude of the reflections mentioned before, caused by the decrease in the P-wave velocity after substituting brine by methane. As is shown by the graph in the right corner of Figure 12b, there is a small increment of the AVO response after fluid substitution.

Comparing the well logs in Figure 12a and Figure 12b, there is an important decrease of the P-wave velocity. The average velocity for the coalbeds saturated with 100% brine is 2370 m/s and after substituting the brine by methane the average P-wave velocity is 1670 m/s. The density log also presents a small decrease after fluid substitution. In the case of the S-wave velocity, a moderate velocity increase occurs as it was expected.

Figure 13 shows the synthetic seismograms generated with a 60 Hz zero phase Ricker wavelet, before and after fluid substitution. The results are similar to the ones generated with the 30 Hz Ricker wavelet but in this case the amplitude variation becomes more evident. With the 60 Hz Ricker wavelet, is still not possible to resolve the Main and Lower seam separately.



**Figure 12. Synthetic seismograms for two coal seams (Main and Lower seam), generated with a 30 Hz zero phase Ricker wavelet. a) coalbeds are saturated with 100% brine, b) coalbeds are saturated with 82% brine and 18% methane.**

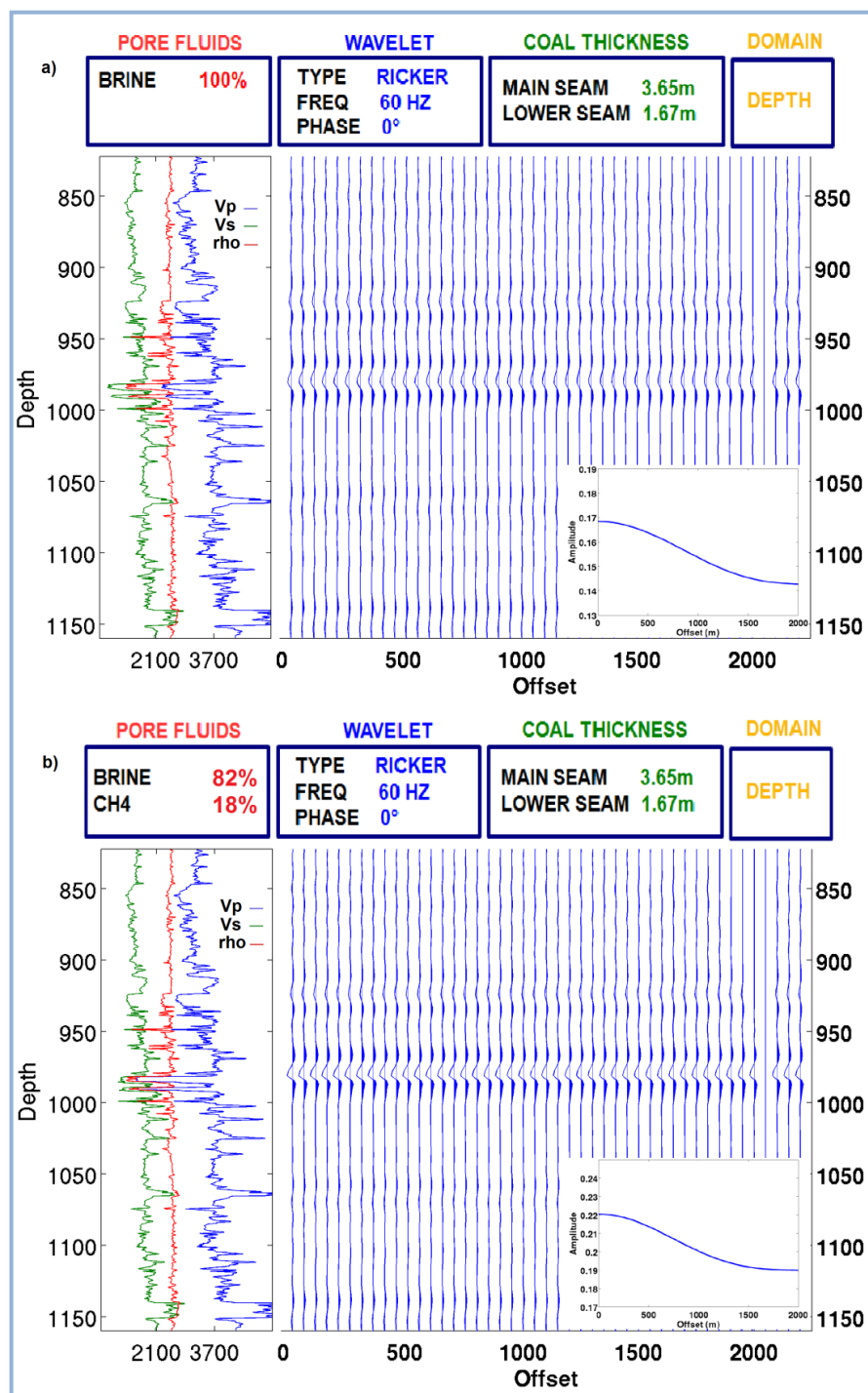


**Figure 13. Synthetic seismograms for two coal seams (Main and Lower seam), generated with a 60 Hz zero phase Ricker wavelet. a) coalbeds are saturated with 100% brine, b) coalbeds are saturated with 82% brine and 18% methane.**

### 3.3.2.2 Case II: Coal seam with a thickness of 10.64 m

In this case, I use the well log data corresponding to the Main Seam and the Lower seam to create a coalbed of 10.64 m thickness. The synthetic seismograms in Figure 14 are generated with a 30 Hz Ricker wavelet. The amplitude trough at a depth of 980 m coincides with the top of the coalbed while the peak at around 990 m can be associated with the base of the coalbed. In this case the reflections seem to be stronger compared with their equivalents in Case I. In addition, AVO response is still not significant.

In the synthetic seismograms in Figure 14a the fluid in the coalbed is 100% brine, and the top and the base of the coalbed can be easily identified as the strongest reflections in the seismograms. Figure 14b shows the synthetic seismograms for the coalbed saturated with a mix of brine and methane. The replacement of brine by methane using Gassmann fluid substitution (Gassmann, 1951) caused a change in the character of the wavelet, presenting an increase in amplitude and a phase shift.

Figure 15 shows the synthetic seismograms generated with the 60 Hz Ricker wavelet. The reflections associated with the top and base of the coal seam are at a depth of 980 m and 990 m respectively, and an AVO response is observed as a decrease of the amplitude with the offset. The variations in character of the wavelet, in terms of amplitude and phase, are evident after fluid substitution.

### 3.3.2.3 Case III: Coal seam with a thickness of 21.28 m

In this case, the data of the coalbed in the case II is duplicated to create a coalbed with a thickness of 21.28 m.

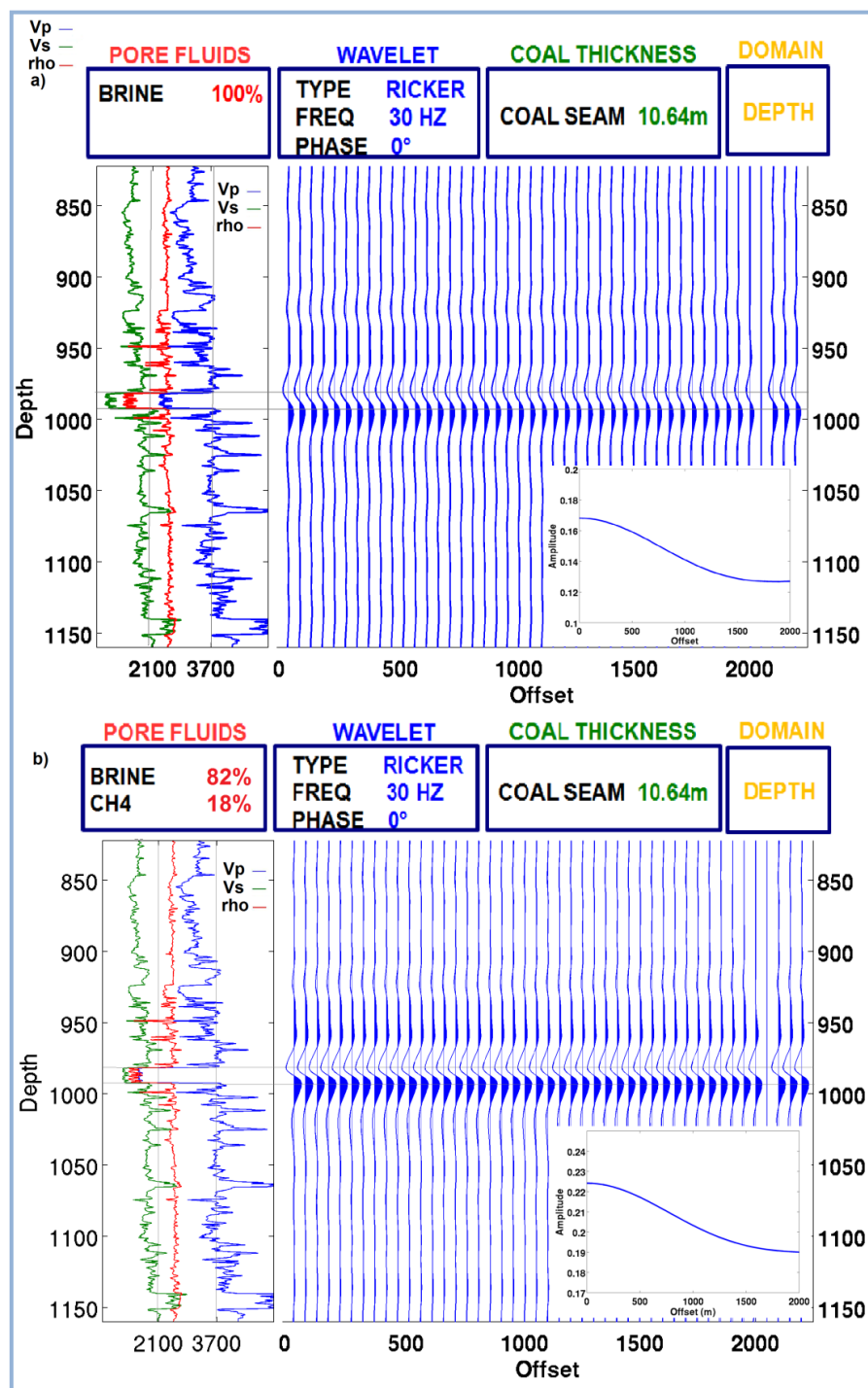


Figure 14. Synthetic seismograms for a 10.61 m coalbed, generated with a 30 Hz zero phase Ricker wavelet. a) coalbeds are saturated with 100% brine, b) coalbeds are saturated with 82% brine and 18% methane.

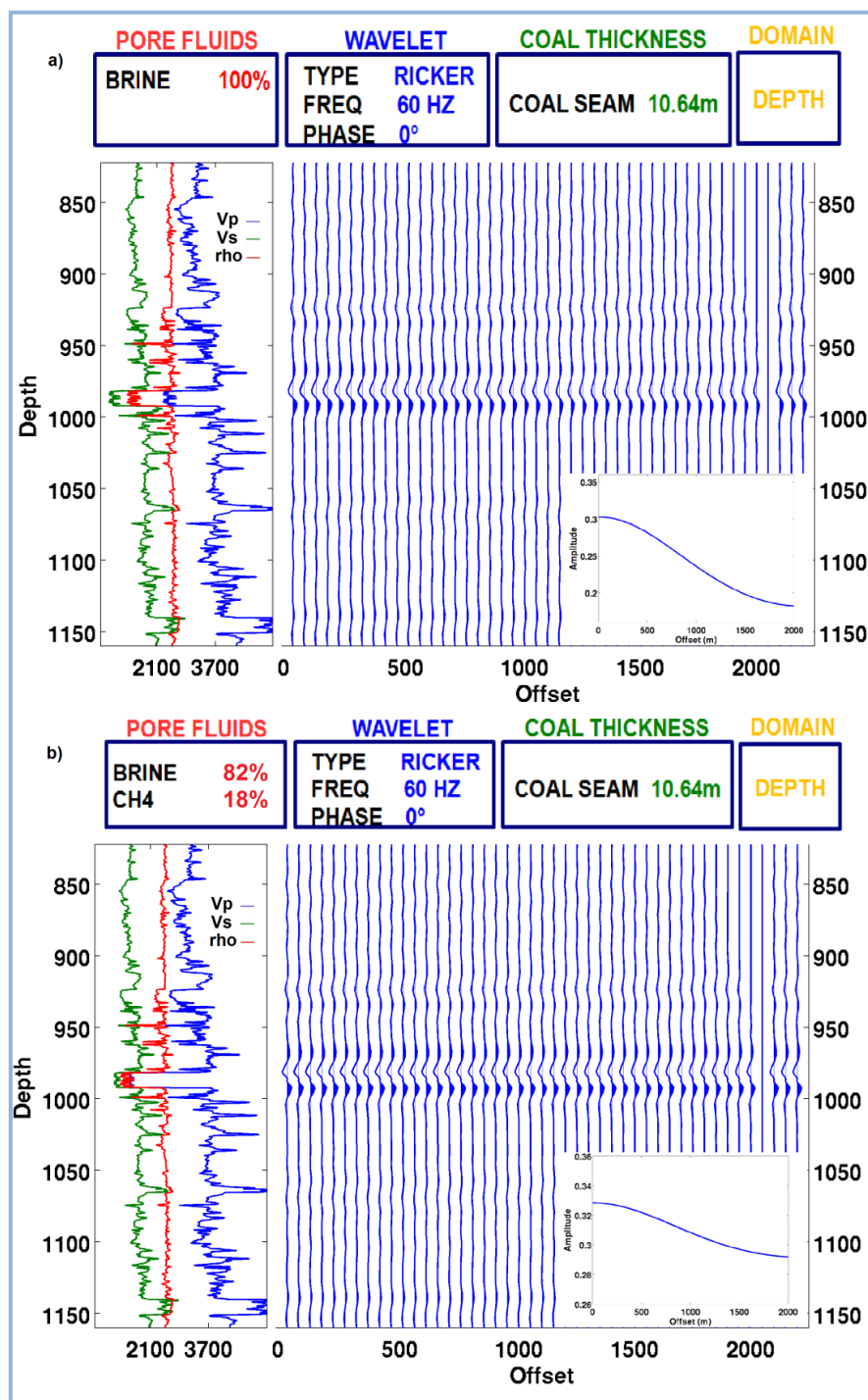


Figure 15. Synthetic seismograms for a 10.61 m coalbed. Generated with a 60 Hz zero phase Ricker wavelet. a) coalbeds are saturated with 100% brine, b) coalbeds are saturated with 82% brine and 18% methane.

Figure 16 displays the synthetic seismogram associated to the response of a 21.28 m coalbed, generated with a 30 Hz zero phase Ricker wavelet. Before fluid substitution (Figure 16a), at approximately 980 m appears the reflection of the top of the coalbed while the one related to the base is close to a depth of 1000 m. These reflections have bigger amplitude compared with their equivalent in Case I and Case II. Also, there is an AVO response associated to a decrease in amplitude with offset.

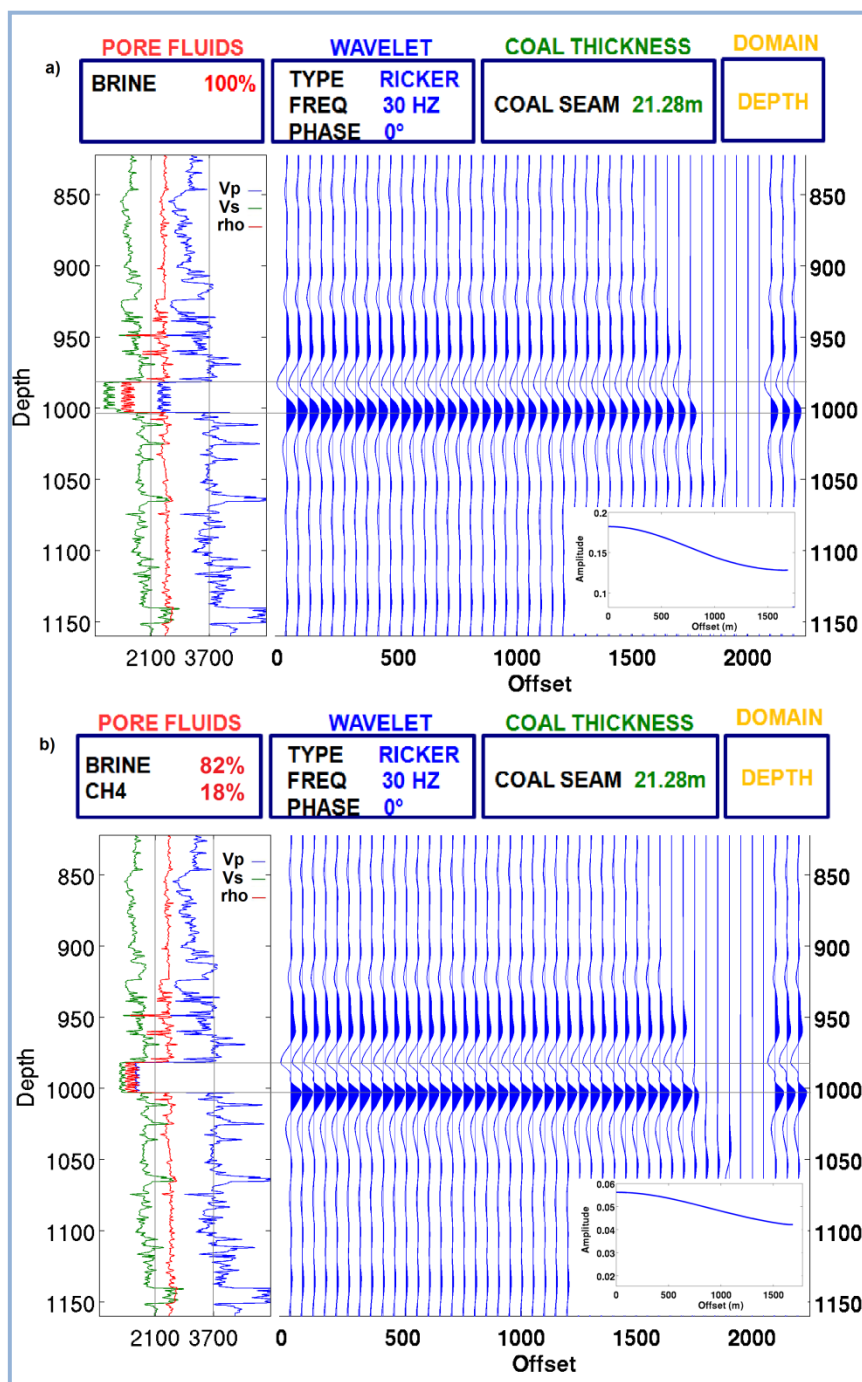
After fluid substitution (Figure 16b), the character of the wavelet completely change presenting a lightly increase of the amplitude of the reflections and a shift in the phase. The AVO response becomes less obvious after substituting brine by methane.

Figure 17 shows the synthetic seismograms generated with a 60 Hz zero phase Ricker wavelet. In these synthetic seismograms, the coalbed is clearly resolved and defined by strong reflections associated with the top and base. In this case, an AVO response is not observed. In Figure 17a, this reflection has small amplitude while in Figure 17b, this reflection show an increase of the amplitude due to the effect of the fluid substitution.

### ***3.3.3 CREWES Zoeppritz equation***

The CREWES Zoeppritz (CREWES.org) explorer is used to evaluate the variations of the reflection coefficients with the incidence angle.

An average of  $V_p$ ,  $V_s$  and density of the coalbed and the overburden are calculated and used in the CREWES Zoeppritz explorer. Table 8 presents these parameters.



**Figure 16. Depth domain synthetic seismograms for a 21.28 m coalbed, generated with a 30 Hz zero phase Ricker wavelet. a) coalbeds are saturated with 100% brine, b) coalbeds are saturated with 82% brine and 18% methane.**

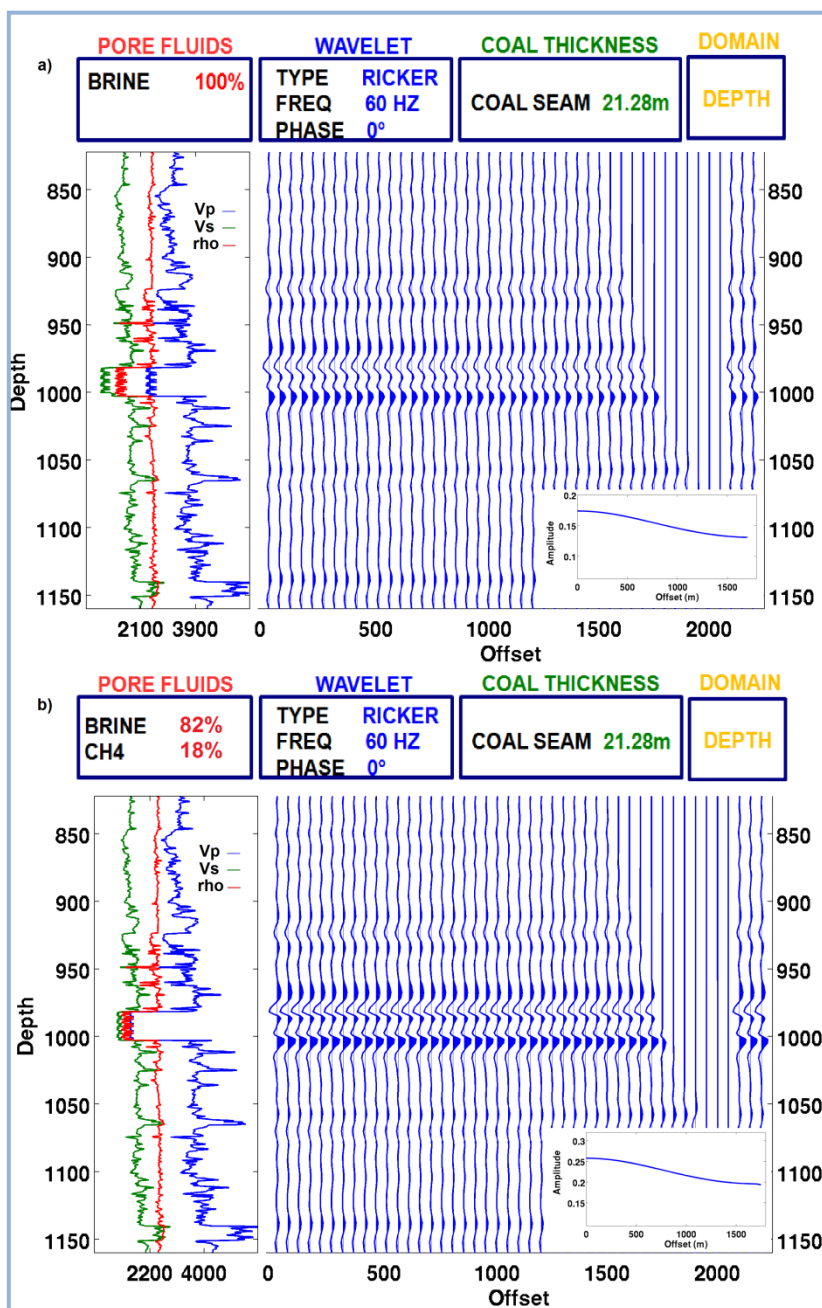
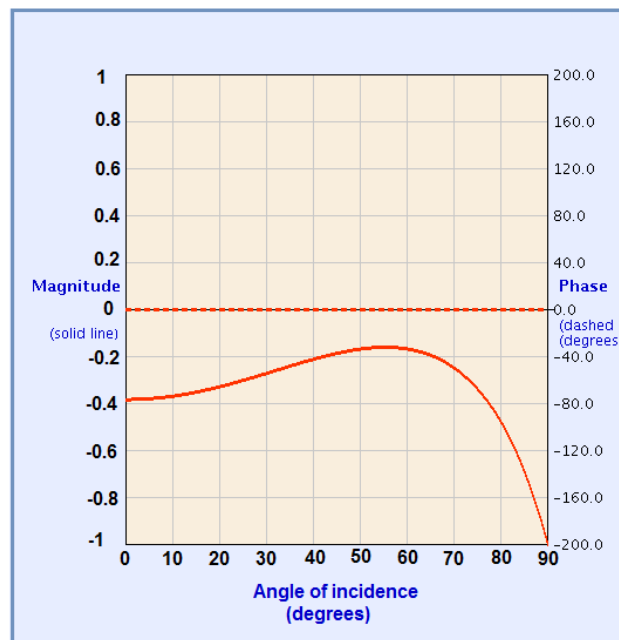


Figure 17. Synthetic seismograms for a 21.28 m coalbed, generated with a 60 Hz zero phase Ricker wavelet. a) coalbeds are saturated with 100% brine, b) coalbeds are saturated with 82% brine and 18% methane.

**Table 8. Parameters for CREWES Zoeppritz explorer**

<b>Parameters for CREWES Zoeppritz explorer</b>	
<b>Overburden:</b>	
$V_p$	3162 m/s
$V_s$	1525 m/s
Density	2432 kg/m <sup>3</sup>
<b>Coalbed:</b>	
$V_p$	2377 m/s
$V_s$	873 m/s
Density	1436 Kg/m <sup>3</sup>

The evaluation of the Zoeppritz equation using the data mentioned before is presented in Figure 18.



**Figure 18. CREWES Zoeppritz explorer (CREWES.org). Upper layer corresponds to an average of the overburden parameters and the lower layer is the coalbed.**

From this graph, it can be interpreted that there is not a critical angle over which the reflection coefficient becomes or approximates to zero. For incidence angles between  $0^\circ$  and  $55^\circ$  the amplitude will tend to slowly decrease and for incidence angles over that range the amplitude will have a representative increase.

Another important observation is that the reflection coefficients have a negative range indicating that in this case the top of the coalbed will be always a trough which coincides with the observation in synthetic seismograms generated.

### **3.4 Summary**

The evaluation of the synthetic seismograms generated with 30 Hz and 60 Hz Ricker wavelets, for different coalbed thicknesses gives an idea of the changes that can be expected depending on the fluid in the pore space of the coalbed. In this chapter, three cases are evaluated: Corbett Field case (Main seam of 3.65 m and Lower seam of 1.67 m), a coal seam of 10.64 m of thickness and a 21.28 m coal seam. As a result, it is observed that it is necessary to have at least a 10 m coalbed to be able to resolve it and identify representative changes in the seismic response due to the replacement of brine by methane. The substitution of brine by methane cause a change in the character and phase of the wavelet and in terms of AVO there is decrease of the amplitude with offset.

## **Chapter 4. Elastic Impedance analysis for methane and CO<sub>2</sub> discrimination in coalbeds. Fruitland coals, San Juan Basin**

In this chapter, I present a methodology to evaluate the use of Elastic Impedance and Elastic Impedance Coefficient to discriminate coals saturated with methane from coals saturated with CO<sub>2</sub>. Also, I evaluate the possibility of monitoring the movement of the CO<sub>2</sub> flood by using these attributes. This methodology is applied to a dataset of the Fruitland coals Fairway, in the north of the San Juan Basin U.S, which is considered the most productive reservoir of coalbed methane in the world.

### **4.1 Area of study**

For the development of this chapter, data that corresponds to the coalbeds of the Fruitland Formation is selected, more specifically in the Fruitland Fairway located in the north part of the San Juan Basin.

The San Juan Basin is located in the western part of the United States of America and extends through the SW of Colorado and the NW New Mexico State (Magill et al., 2010), covering an area of approximately 38000 km<sup>2</sup> (Laubach and Tremain, 1991).

The structure of the San Juan Basin is defined by the Laramide Orogeny, between the Late Cretaceous and the Eocene (Kaiser and Ayers, 1994), which caused the generation of folds and faults along the boundaries of the basin. The San Juan Basin is interpreted as an asymmetrical syncline having its axis in the south border of Colorado State. The limits of the San Juan Basin are determined by the Hogback Monocline to the north, the Defiance Monocline to the SW and the Zuni Uplift to the south (Crist et al., 1989). Figure 19 shows the extension and limits of the San Juan Basin.

The San Juan Basin presents sediment fill of continental and marine origin, deposited during the Cretaceous and the early Tertiary (Laubach and Tremain, 1991) and they are associated with cycles of transgressive-regressive deposition. The dominant lithologies in this basin are shale, siltstone and sandstone with a less significant presence of coal and limestone (Michael et al., 1993). The natural gas production from Fruitland coal in the San Juan Basin started in 1986 (Magill et al., 2010), and since that moment it has become a significant source of natural gas for the U.S.

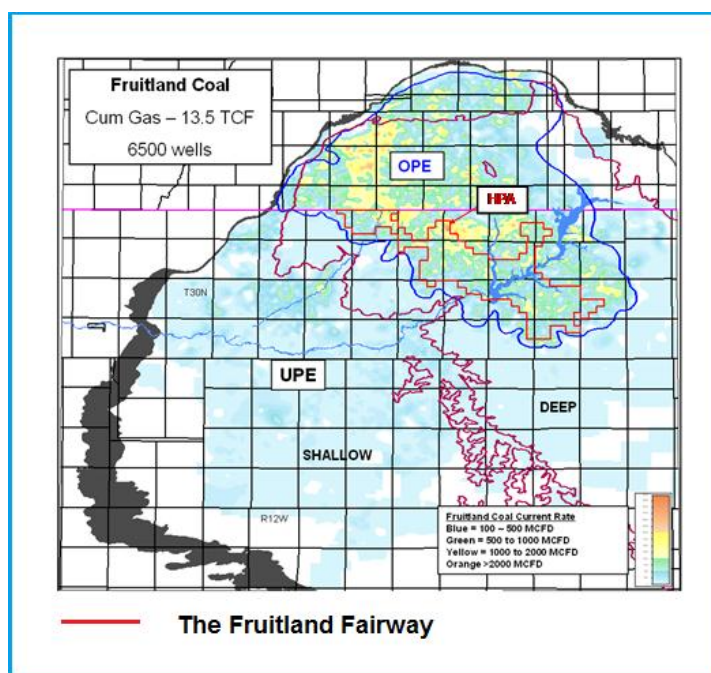


**Figure 19. San Juan Basin map. Red line shows the limits of the Fruitland Fairway.**

In the north of the San Juan Basin, there is an area called the Fruitland coals Fairway (Magill et al., 2010) with an extension that corresponds to 15% of the coalbed methane productive zones in the basin. The coal Fairway is an over-pressured area, characterized by the presence of thicker coalbeds in the Fruitland Formation (Jenkins et al., 2008), with higher coal rank, lower ash content, better developed cleat systems (Magill et

al., 2010) and higher permeability in the range of 20-100 mD. The Coal Fairway is recognized by being the most productive reservoir of coalbed methane in the world and is responsible of approximately 75% of the coalbed methane produced from the San Juan Basin (Jenkins et al., 2008). The red line in Figure 19 delimitates the Fruitland Fairway location in the San Juan Basin.

#### ***4.1.1 Fruitland Formation***

The deposition of the Fruitland Formation occurred in the Late Cretaceous (Snyder et al., 2003) and it is mainly composed of shale, siltstone, sandstone and coal. The deposition of this formation is associated with one of the regressive cycles that took place in the San Juan Basin (Michael et al., 1993) and can be interpreted as occurring over a 7 million year period (Pashin, 1998 ).

The Lewis Shale and the Pictured Cliffs Sandstone Formations underlie the Fruitland Formation. These formations were deposited in an open marine and a shore face environment respectively, and are associated with a highstand system track. The Lewis Shale and the Picture Cliffs Formations present sediments, which become coarser to the upward direction, and have a thickness of approximately 400 m (Pashin, 1998). A retreat of the sea during the Late Cretaceous, led to the deposition of coastal sediments that form the Fruitland Formation (Snyder et al., 2003) (Laubach and Tremain, 1991). Conformably, the sandstones and shales that form the Kirtland Shale Formation were deposited overlying the Fruitland Formation. Having a thickness of approximately 200 m (Pashin, 1998), the Kirtland Shale has been interpreted as a regional seal (Oudinot et al., 2009).

Figure 20 shows a depositional sequence of the San Juan Basin during the upper Cretaceous.

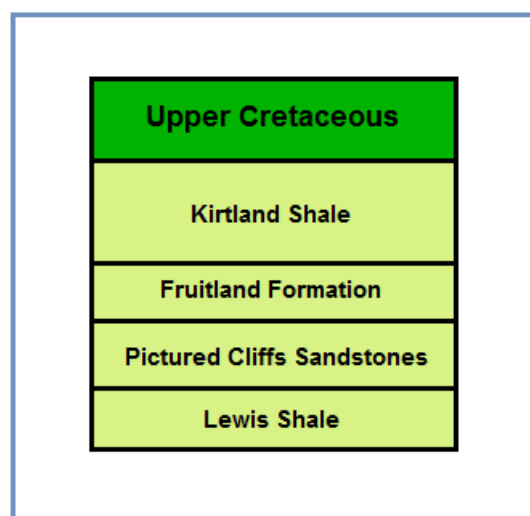


**Figure 20. Depositional sequence of the Upper Cretaceous in the San Juan Basin.**

The Fruitland Formation has a maximum thickness of approximately 150 m (Michael et al., 1993). It presents its thicker part in the NW area of the San Juan Basin and it becomes thinner and disappears towards the east (Laubach and Tremain, 1991). Laterally discontinuous coalbeds of up to 12 m thickness constitute the Fruitland Formation (Michael et al., 1993) with approximately 30 m of coal total net thickness (Jenkins et al., 2008).

The maceral content of Fruitland coals is mostly vitrinite which constitutes approximately 80% of the total macerals; the 20% left corresponds to exinite and inertinite (Michael et al., 1993). Coals from the Fruitland Formation have an ash content of approximately 8-30% (Laubach and Tremain, 1991) with a rank that increases from sub-bituminous to bituminous (low volatile) towards the north direction (Jones, 1984).

The Fruitland coals have cleat porosity between 0.5-2% (Snyder et al., 2003) and in some cases minerals like pyrite, calcite and gypsum partially fill them. The face cleats, which formed earlier than the butt cleats, are well developed and have an extension in the

order of meters. The butt cleats have an extension of 10 cm or less and show an intersection angle of 80-90° with the face cleats (Laubach and Tremain, 1991).

## **4.2 Methodology**

### ***4.2.1 Fluid simulation***

Geological data and production data from the Fruitland coals is collected to develop a proxy model of the Fruitland Coal Fairway in the San Juan Basin.

Initially, a vertical single well model is built in order to evaluate the relative permeability and relative adsorption data that is being used. For this model, the history match is performed using production data from this well and dynamic data is included.

Based on this single well model, a reservoir model is built. The reservoir model is developed with a grid dimension of 175x175x1, and producing wells on 320-acre spacing. For this project, a single coalbed layer with a thickness of 15.24 m (50 ft) at a depth of 914.4 m (3000 ft) is modeled over an extension of 31.4 km<sup>2</sup>.

The inputs for the generation of the reservoir model are:

- Historical gas production and water production
- Relative permeability curve associated with the Fairway area
- Langmuir isotherms for CO<sub>2</sub> and methane
- A function that determines the absolute permeability growth in terms of reservoir pressure (Clarkson, personal communication)
- Relative adsorption data for CO<sub>2</sub> and methane calculated with the Extended Langmuir model.

Table 9 presents the Langmuir parameters and Table 10 shows the model assumptions.

**Table 9. Langmuir parameters**

<b>Langmuir Parameters</b>	
Langmuir volume $V_L$ CH <sub>4</sub>	472 scf/ton
Langmuir pressure $P_L$ CH <sub>4</sub>	592.2 psia
Langmuir volume $V_L$ CO <sub>2</sub>	689 scf/ton
Langmuir pressure $P_L$ CO <sub>2</sub>	259.3 psia

**Table 10. Reservoir model assumptions**

<b>Model assumptions</b>	
Coal thickness	15.24 m (50 ft)
Top of the coalbed	914.4 m (3000 ft)
Grid size	175x175x1
Area of study	31.4 km <sup>2</sup>
Absolute permeability	80 mD
Initial pressure	1616 psia (11.14 MPa)
Temperature	41.66 °C
Fracture porosity	0.0035 (fraction)
Initial water saturation	100%
Skin	0

Using the reservoir model, the production forecast of primary depletion for 24 wells in the area of study is performed. The production forecast started in 1999 and extends until 2031.

This model is also used to forecast ECBM production by CO<sub>2</sub> injection. In this case, four CO<sub>2</sub> injection wells are added to the model. It is assumed that the injection started in July 2003, is shut in October 2010, and the forecast is for continuous injection until 2031.

#### 4.2.2 Data selection

$V_p$ ,  $V_s$  and density values needed to perform the fluid substitution are selected from well log data available for different fields in the San Juan Basin (Figure 21 and Figure 22).

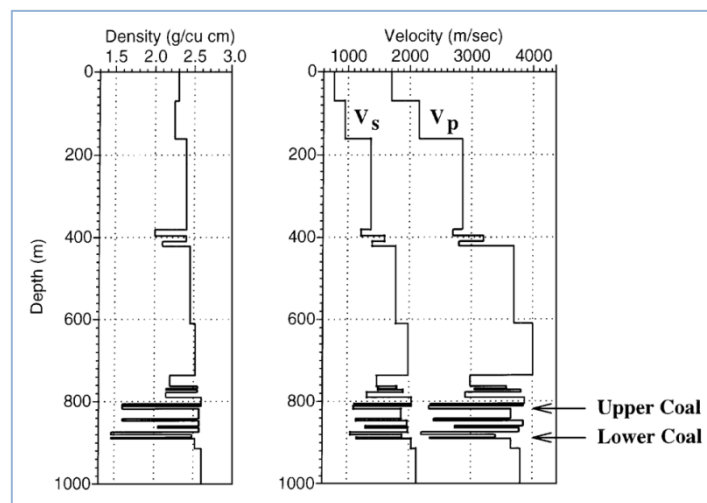


**Figure 21.  $V_p$ ,  $V_s$  and density model from the Hamilton 3 well, Cedar Hill, San Juan Basin (Figure 8, Ramos and Davis, 1997).**

The selection of  $V_p$  is based on an average of the slowness associated with coals, observed on the sonic log of the Glover Well, located in the Archuleta County in the San Juan Basin (Jones et al., 1984). For the selection of  $V_p$ , we also use a velocity model generated for the Hamilton 3 well, which is based in a sonic log that was run in this well (Figure 21).

The  $V_s$  velocity used for the fluid substitution is selected by doing an average of the shear velocities associated to coalbeds in the velocity model of the Hamilton 3 well (Figure

21). Averages of the velocities associated with the upper and lower coalbed are taken into account.

In the case of the density, an average of the coal densities obtained from bulk density logs of 4 wells located in Pump Canyon is used, inside the Fairway in the San Juan Basin (Figure 22).

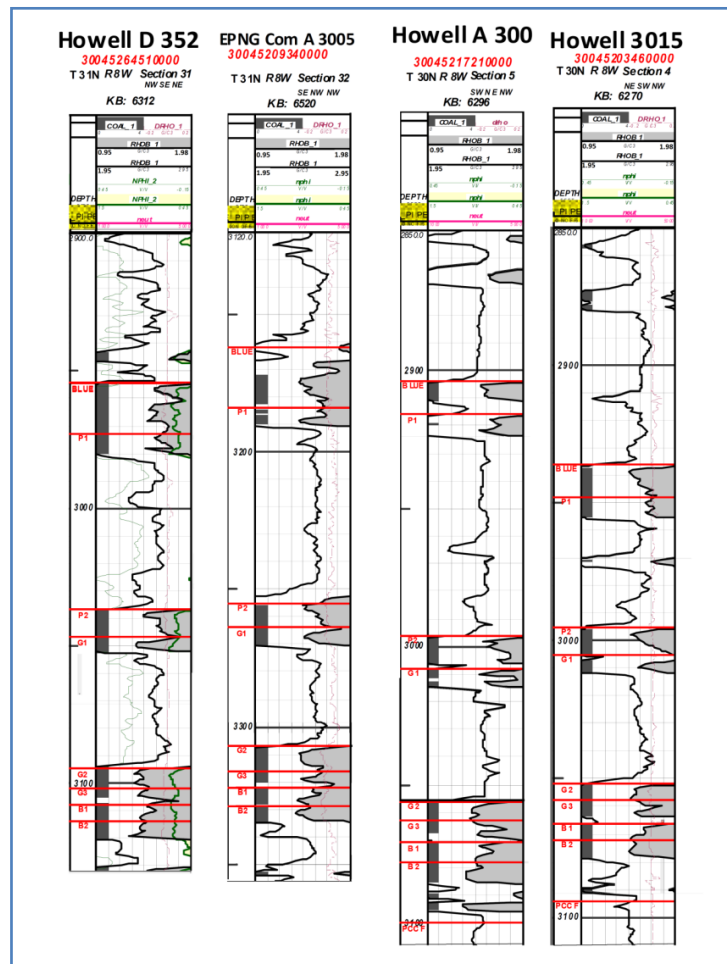


**Figure 22. Density logs. Pump Canyon, San Juan Basin (Modified from Figure 5, Koperna et al., 2009).**

Table 11 present the values of  $V_p$ ,  $V_s$  and density used in this study to perform the fluid substitution.

**Table 11.  $V_p$ ,  $V_s$  and density selected values**

<b>Parameters for fluid substitution</b>	
$V_p$	2450 m/s
$V_s$	1025 m/s
Density	1.6 g/cm <sup>3</sup>

### 4.2.3 Gassmann fluid substitution

The Gassmann fluid substitution is performed by using the values of  $V_p$ ,  $V_s$  and density selected from the well log data available in the area of study (Table 11).

In this case, in order to calculate the bulk modulus of the frame of the dry rock,  $K^*$ , the results presented by Yu et al. (1993) are used. In their paper, after performing laboratory tests, they conclude that the bulk modulus of the dry rock corresponds to approximately 15% less than the bulk modulus of the same rock saturated with water (Yu et al., 1993). Therefore,  $K^*$  is calculated according to:

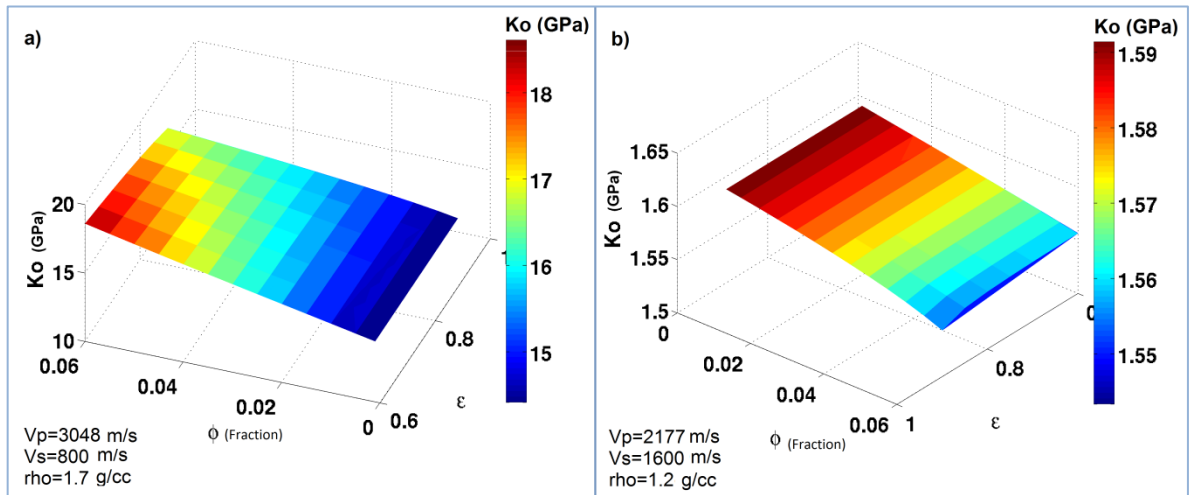
$$K^* = 0.85K_{sat} . \quad (41)$$

The calculation of the bulk modulus of the mineral matrix is more complicated since the standard procedures are not applicable for coals. In order to estimate an appropriate value for our area of study, possible values for  $K_0$ , using limit values of  $V_p$ ,  $V_s$  and density associated with coals are evaluated. To do this, a graph with the variation of the bulk modulus of the mineral matrix with the porosity ( $\phi$ ) and a parameter epsilon is presented in Figure 23 and Figure 24. The parameter epsilon is defined as:

$$K^* = \varepsilon K_{sat} . \quad (42)$$

For these calculations, epsilon varies between 0.6 and 0.9 and the porosity is in the range of 0.001-6%. The bulk modulus of the mineral matrix was calculated using equation 6.

Figure 23 present the variation of  $K_0$  with respect to  $\epsilon$  and the porosity for maximum and minimum  $V_p$  associated with coals.



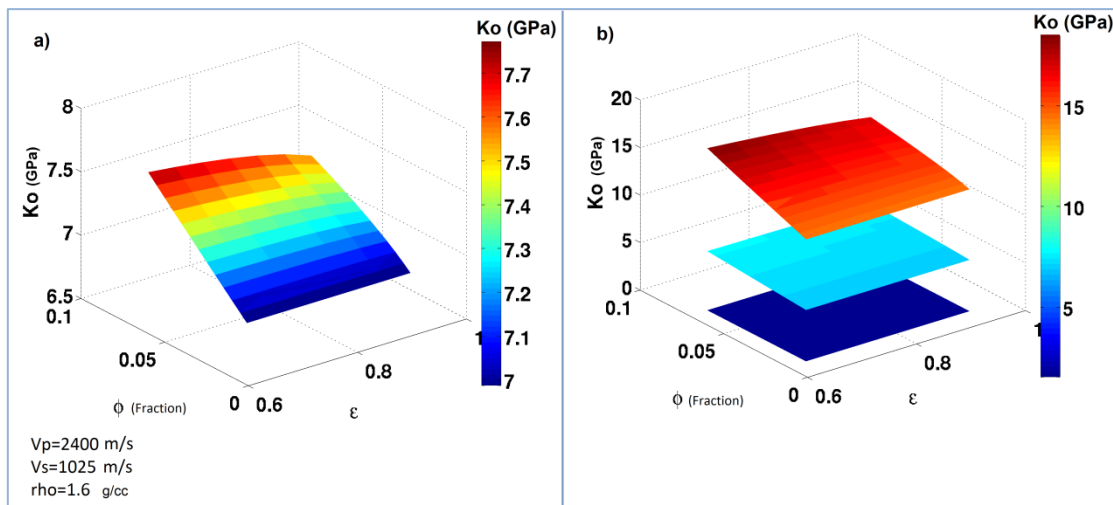
**Figure 23. Dependence of the mineral matrix bulk modulus with  $\epsilon$  and  $\phi$  a) using maximum  $V_p$  value associated with coals, b) using minimum  $V_p$  value associated with coals.**

Figure 23a, corresponds to the variation of  $K_0$  calculated using a  $V_p$  value of 3048 m/s. In this case,  $K_0$  does not present major variations for  $\epsilon$  between 0.6 and 0.9 and porosities of 0.1 and 4%. For the higher porosities (4%-6%),  $K_0$  becomes bigger as  $\epsilon$  decrease. From this graph,  $K_0$  tends to slowly increase from 14 to 18 GPa with the increase of the porosity.

Figure 23b corresponds to the variation of  $K_0$  calculated using a  $V_p$  value of 2177 m/s. In this case,  $K_0$  does not present representative variations when changing  $\epsilon$  from

0.6 to 0.9. In terms of the effects of the porosity, the variation of  $K_0$  is not significant for the range of porosity evaluated, presenting values in the range of 1.54-1.59 GPa.

Figure 24a shows the  $\epsilon$ ,  $\phi$ ,  $K_0$  surface, calculated using the values of  $V_p$ ,  $V_s$  and density in Table 11, which correspond to the values selected for our area of study in the San Juan Basin. As we can see this surface behaves similar to the surface calculated using the maximum  $V_p$  value for coals and in this case,  $K_0$  varies in the range of 6.98-7.77 GPa. Figure 24b present the three surfaces together.



**Figure 24. Dependence of the mineral matrix bulk modulus with  $\epsilon$  and the  $\phi$  a) using  $V_p$ ,  $V_s$  and density values associated with the San Juan Basin, b) comparison of the three surfaces (maximum  $V_p$ , minimum  $V_p$ , San Juan Basin data).**

The  $K_0$  value for this study was selected from the surface presented in Figure 24a, taking into account the values that correspond to a porosity in the range of 0.1-1% and an  $\epsilon$  between 0.8 and 0.9. The selected value for  $K_0$  is 7 GPa.

The fluid properties used to perform the fluid substitution are calculated using Batzle and Wang (1992) equations and the Gassmann fluid substitution is performed following the methodology previously described in chapter 3.

Again, the Gassmann equation is used assuming that the macroporosity system of the coals, which corresponds to the cleats, is the one that governs its permeability. Hence, the cleats porosity is the one used during the fluid substitution.

### **4.3 Results**

#### ***4.3.1 Fluid simulation***

The fluid simulation provides us with data of the reservoir pressure, and methane, CO<sub>2</sub> and water saturation from 2002 until 2031. In this section, reservoir pressure and fluid saturations are presented for three cases of study:

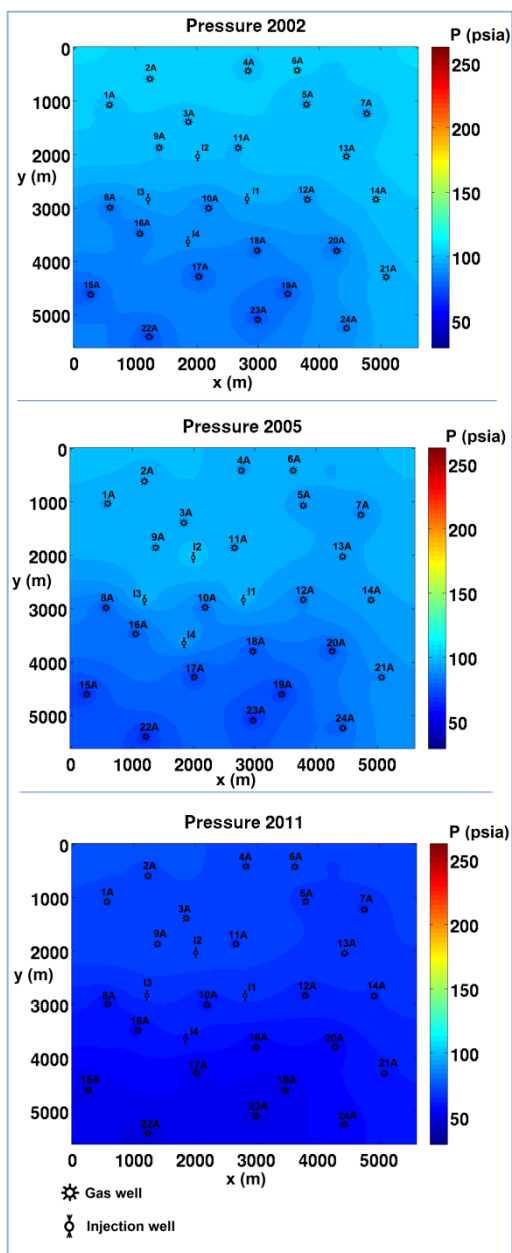
- 2002 model: Primary production case
- 2005 model: Enhanced coalbed methane (ECBM) production by CO<sub>2</sub> injection. Two years after injection started
- 2011 model: One year after stopping CO<sub>2</sub> injection

The pressure map of the reservoir is presented in Figure 25. The reservoir pressure decreases during primary production from an initial pressure of 1616 psia to 100-105 psia in the north section of the area of study, and 80-85 psia towards the south (Figure 25a). The reservoir pressure tends to increase from the SW to the NE. By 2005 (Figure 25b), the reservoir pressure continues decreasing due to depletion. After two years of starting CO<sub>2</sub> injection, the reservoir pressure presents a small increase in the areas around the injection wells. For the 2011 model (Figure 25c), the pressures are in the range of 70-75 psia to the

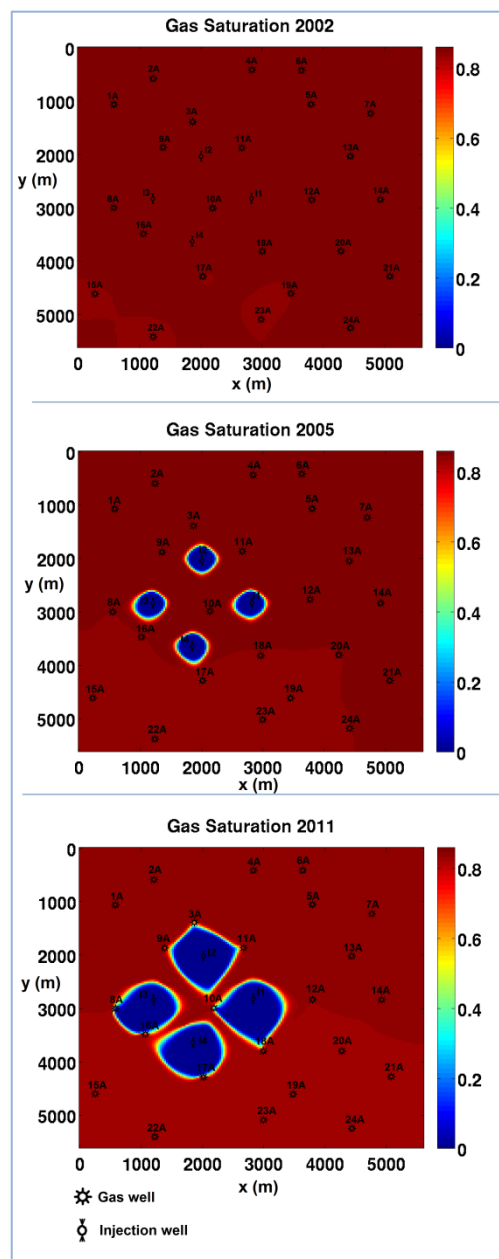
north and 52-60 psia to the south. The reservoir pressures decrease with time due to production activities.

Figure 26 presents the methane saturation along the area of study for the three cases that are being evaluated. Figure 26a, which is the one that corresponds to the primary production case, shows a high saturation of methane over the complete area of study, more specifically around 80% of methane saturation with uniform distribution over the area. Figure 26b shows methane saturations after 2 years of injection of CO<sub>2</sub> into the coalbed. In this figure, it is possible to appreciate a decrease in the methane saturation around the injection wells. In the zones surrounding the injectors, the footprint of the CO<sub>2</sub> injection is identified presenting a radial distribution. In these zones, there is a reduction of the methane saturation from 80% (2002 model) to less than 15%. The 2011 model is presented in Figure 26c. One year after finishing the CO<sub>2</sub> injection, the CO<sub>2</sub> flood is still evident in the saturation maps. The area affected by the CO<sub>2</sub> injection has expanded through the years and in these zones the methane saturation is close to 10%. The distribution of the CO<sub>2</sub> flood around the injection wells does not present a radial distribution anymore and it seems to be displacing to the south where lower pressures are dominant.

The CO<sub>2</sub> saturation is presented in Figure 27. In the 2002 model (Figure 27a), which is associated to primary production case, the presence of CO<sub>2</sub> in the area is homogeneously distributed and present values around 18-20%. Figure 27b presents the increase of CO<sub>2</sub> saturation in the vicinities of the injection wells as consequence of the injection process. An increase of the CO<sub>2</sub> saturation from 20% to 85% or more is observed. In the 2011 model (Figure 27c), the displacement of the CO<sub>2</sub> footprint to the south of the area of study is observed, presenting ~85% of CO<sub>2</sub> saturation in these zones.



**Figure 25. Reservoir pressure.**  
**a) Primary production (2002),**  
**b) ECBM by CO<sub>2</sub> injection (2005), and**  
**c) one year after shutting the injection wells (2011).**



**Figure 26. Methane saturation.**  
**a) Primary production (2002),**  
**b) ECBM by CO<sub>2</sub> injection (2005), and**  
**c) one year after shutting the injection wells (2011).**

Figure 28a represents a coalbed that has been dewatered and presents water saturation in the order of  $10^{-2}\%$ . The water saturation at this stage tends to increase from SW to NE. The water saturation also has been affected by the  $\text{CO}_2$  injection; it is possible to appreciate the footprint created by the displacement of water due to  $\text{CO}_2$  injection (Figure 28b and Figure 28c). The water saturation continuously decreases specially in the areas surrounding the injection wells and along the rest of the area of study the water saturation seems to keep the same trend.

#### ***4.3.2 Gassmann fluid substitution***

In this section, the changes in  $V_p$ ,  $V_s$  and density due to depletion and  $\text{CO}_2$  injection in a 50 ft coalbed are evaluated. As an initial state, it is assumed that the coalbed is fully saturated with brine and the initial values of  $V_p$ ,  $V_s$  and density are presented in Table 11.

Figure 29 presents the changes in  $V_p$ . In this case,  $V_p$  decrease from the initial value of 2450 m/s to a range of 2390-2395 m/s when replacing brine by methane in the pore space (Figure 29a). In the velocity map presented in Figure 29a,  $V_p$  tends to slowly increase from SW to NE. After  $\text{CO}_2$  injection it is observed that, in the area around the injection wells, there is an area of lower velocity associated with the increase of  $\text{CO}_2$  saturation (Figure 29b). After shutting injection wells, the  $\text{CO}_2$  flood seems to be moving to the south, where the area presents the lower pressures, and this is also evident in the velocity map in Figure 29c. In this case, it is observed a decrease in  $V_p$  along the complete area of study that can be associated to depletion. The lowest velocities are in the south and this can be related to a decrease in the methane saturation and lower pressures in this zone (Figure 29c).

$V_s$  has a more homogeneous distribution than  $V_p$  (Figure 30). After replacing brine by methane, the change in  $V_s$  is not relevant. The footprint of  $\text{CO}_2$  injection in the coalbed

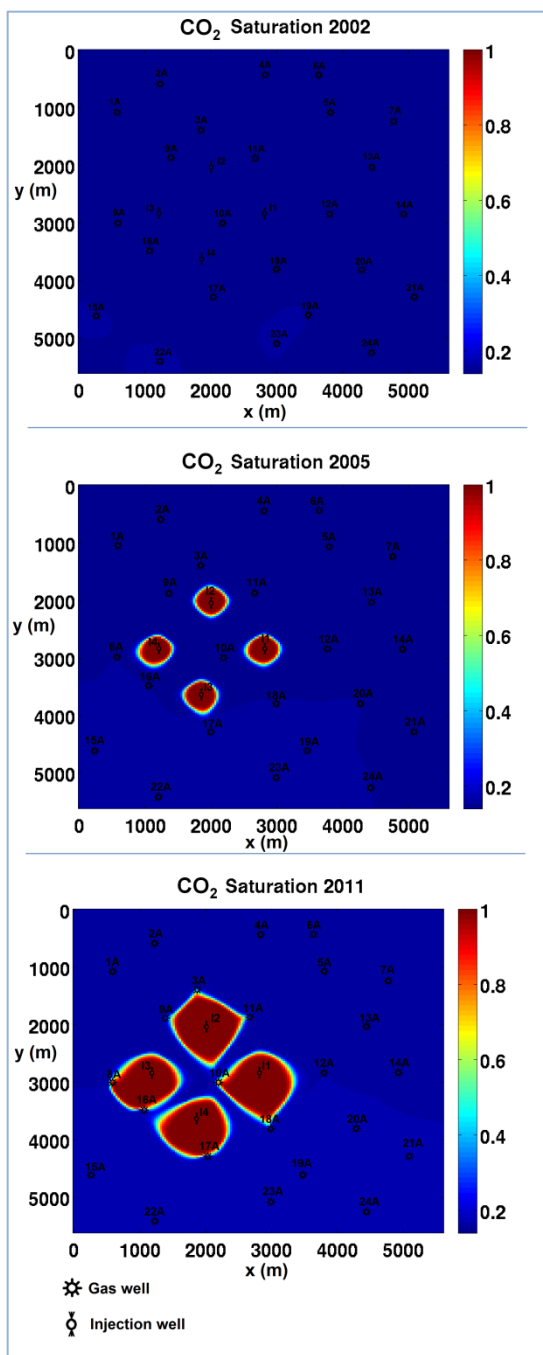


Figure 27. CO<sub>2</sub> saturation a) Primary production (2002); b) ECBM by CO<sub>2</sub> injection (2005), and c) one year after shutting the injection wells (2011).

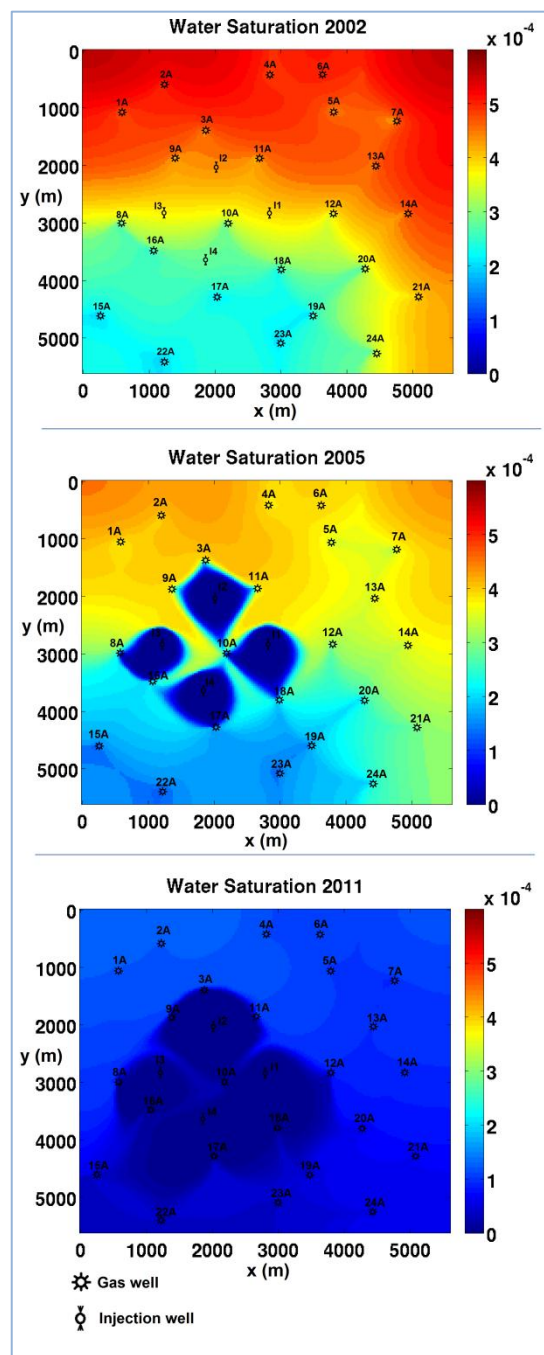


Figure 28. Water saturation. a) Primary production (2002); b) ECBM by CO<sub>2</sub> injection (2005), and c) one year after shutting the injection wells (2011).

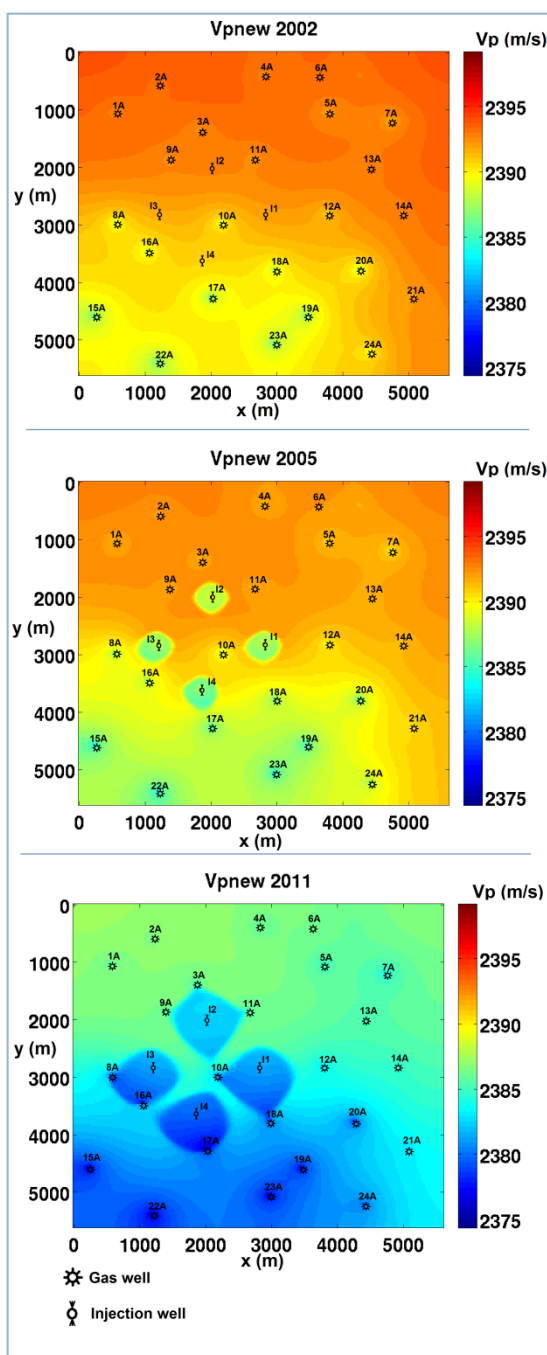


Figure 29.  $V_p$  a) Primary production (2002), b) ECBM by  $\text{CO}_2$  injection (2005), and c) one year after shutting the injection wells (2011).

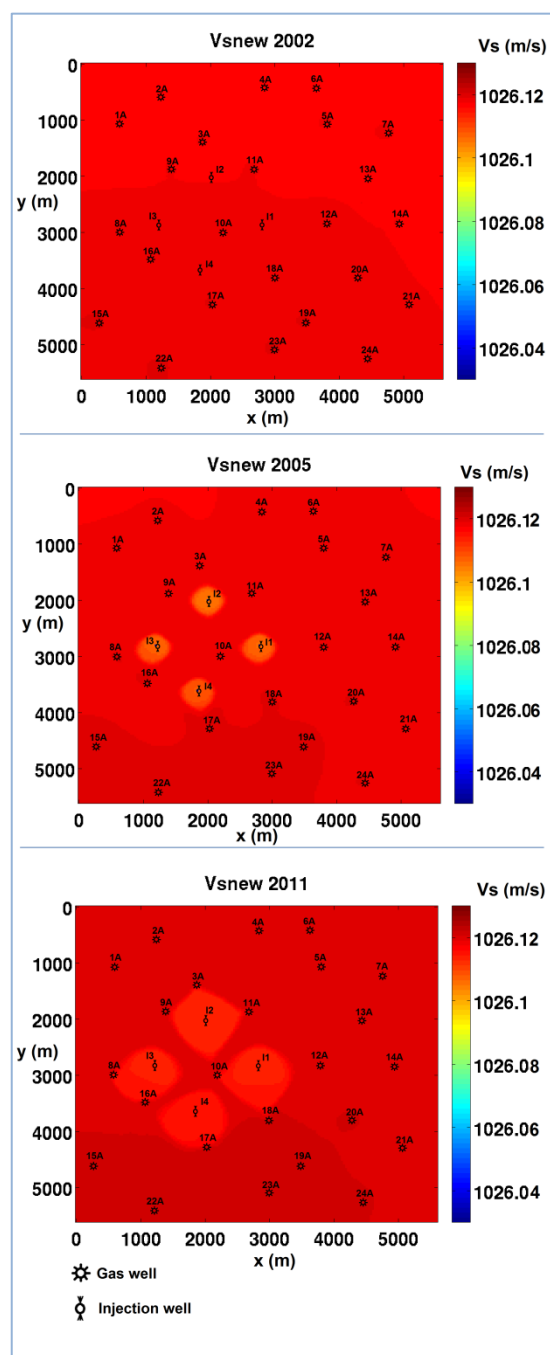
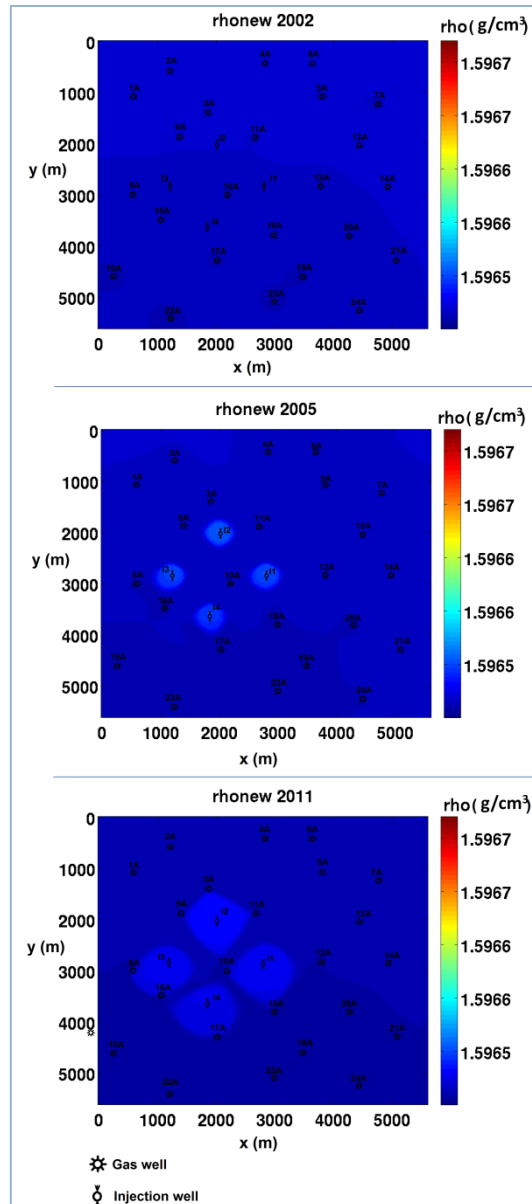


Figure 30.  $V_s$  a) Primary production (2002), b) ECBM by  $\text{CO}_2$  injection (2005), and c) one year after shutting the injection wells (2011).

is also evident in the shear wave velocity map but the magnitudes of the changes are not significant (Figure 30b and Figure 30c). The bulk density presents a similar behavior to  $V_s$  and the magnitudes of the density changes are not meaningful as well (Figure 31b and Figure 31c).



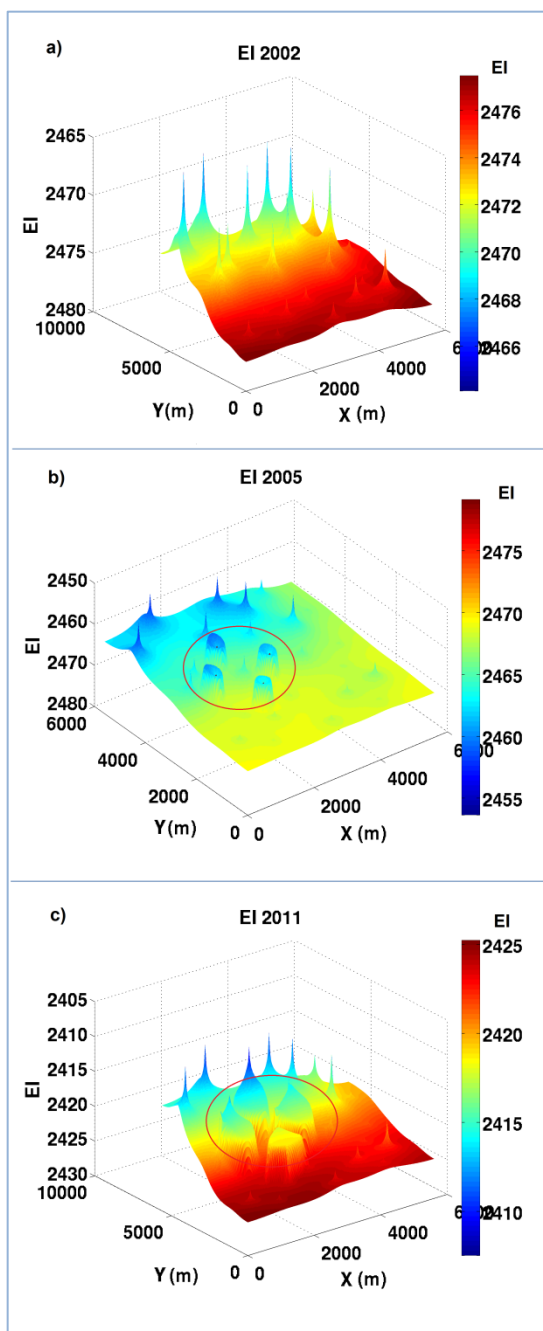
**Figure 31. Bulk density a) Primary production (2002), b) ECBM by  $\text{CO}_2$  injection (2005), and c) one year after shutting the injection wells (2011).**

### 4.3.3 Impedance analysis

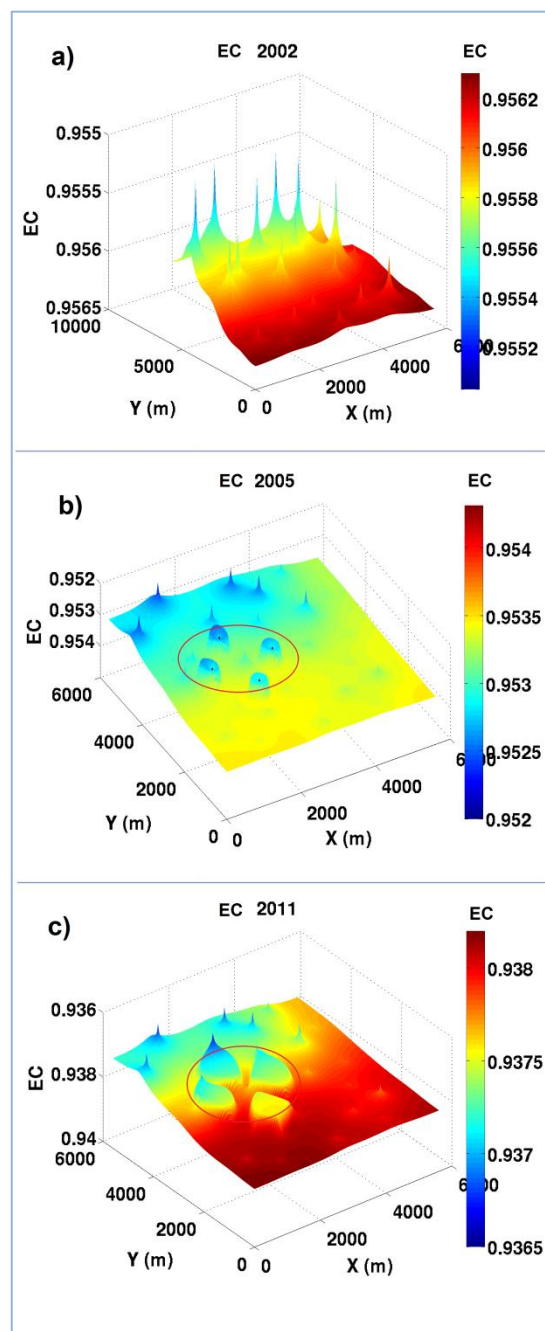
Elastic Impedance (EI) and Elastic Impedance Coefficient (EC) are used to attempt to discriminate methane from CO<sub>2</sub> in coalbeds. These results are presented in Figure 32 and Figure 33.

Figure 32a presents the EI for the area of study before the CO<sub>2</sub> injection started (2002 model). Figure 32a shows a decrease of the EI from south to north and along the area of study, peaks of low EI are observed. These peaks of low EI are associated to the location of the 24 wells in the area of study. The decrease of the EI in the areas surrounding each well is consequence of the decrease of the compressional wave velocity in that area due to changes in the fluid saturations and a reduction of pressure in these areas. The wells located in the northern part of the area of study produce a stronger response and these can be associated to the presence of higher pressure values and methane saturation towards the north. Figure 33a shows the response of the EC of the Fruitland coals in the area of study. The result is similar to the one obtained with the EI with a tendency to decrease from south to north.

Figure 32b shows the EI response two years after starting CO<sub>2</sub> injection. In this figure, the low EI response in the vicinity of the well locations and the EI tendency to decrease from south to north is still observed. In this case, it is also possible to observe the path of the flood of CO<sub>2</sub> that has been injected. In the area inside the red circle, there are four zones of low EI that corresponds to the vicinities of the injection wells and the areas of higher CO<sub>2</sub> saturation in that period of time (2005). In the exact location of the four injection wells, there is a local high in the EI response that is associated to the changes in the fluid saturations and the pressure due to injection (Figure 32b).



**Figure 32. EI a) Primary production (2002), b) ECBM by CO<sub>2</sub> injection (2005), and c) one year after shutting the injection wells (2011).**



**Figure 33. EC a) Primary production (2002), b) ECBM by CO<sub>2</sub> injection (2005), and c) one year after shutting the injection wells (2011).**

Figure 33b presents the EC response. The red circle delineates the area affected by CO<sub>2</sub> injection and the EC low response associated with the CO<sub>2</sub> flood. Similar results to the EI can be observed with EC but with less detail. The EC seems to delineate better the changes that are consequence of CO<sub>2</sub> injection.

Figure 32c and Figure 33c show the EI and EC response of the area of study, one year after stopping CO<sub>2</sub> injection. In Figure 32c, the zones of injection have a low EI response and the footprint of the displacement of the CO<sub>2</sub> injected is evident (red circle). With the EC (Figure 33c), the effects of the CO<sub>2</sub> injection seems to be the most relevant changes in the area of study, presenting lower values of EC than the surrounding areas. In this case EC highlight more the CO<sub>2</sub> footprint than the EI. With both, EI and EC, it is possible to observe how the areas affected by the injection have become bigger and how the CO<sub>2</sub> flood has propagated in the area of study.

The changes in EI and EC that are observed in the area of study allow us to monitor the movement of the CO<sub>2</sub> that has been injected, through the coalbed. However these attributes did not provide a good discrimination between the coalbed saturated with CO<sub>2</sub> and saturated with methane. In Figure 32 and Figure 33 can be observed that the EI and EC values associated with the coalbed saturated with mostly CO<sub>2</sub> are also associated to some zones mostly saturated with methane.

The changes in EI and EC in Figure 32 and Figure 33 are small in magnitude and it is difficult to predict if it will be possible to identify the CO<sub>2</sub> front in seismic data.

#### **4.4 Summary**

The capacity of the Elastic Impedance (EI) and Elastic Impedance Coefficient (EC) to discriminate methane from CO<sub>2</sub> in coalbeds is evaluated in this chapter. The fluid

simulation, the Gassmann fluid substitution and the attribute calculation are performed using a data set from the Fruitland Formation coals in the San Juan Basin. The fluid simulation provided the data required to perform the fluid substitution and estimate changes in  $V_p$ ,  $V_s$  and density, associated with CBM primary production and  $\text{CO}_2$ -ECBM. The Gassmann fluid substitution estimates a decrease in  $V_p$  for the CBM and the  $\text{CO}_2$ -ECBM production, while the changes in  $V_s$  and density are not significant. Finally, EI and EC attributes are not able to discriminate methane from  $\text{CO}_2$  but it is possible to monitor the movement of the  $\text{CO}_2$  flood during and after injection.

## **Chapter 5. Conclusions**

### **5.1 Evaluation of time-lapse seismic as a monitoring tool during CBM production**

An evaluation of the seismic response of coalbeds during CBM primary depletion is performed in Chapter 3 of this thesis. This study is done by implementing a methodology which is based on a workflow previously developed by Zarantonello et al. (2010) for the generation of a time-lapse seismic model during CO<sub>2</sub>-ECBM production and using a data set from the Mannville coals in the Corbett Field.

Initially a fluid simulation is performed in order to determine brine and methane saturations at different stages of primary depletion. Based on these fluid saturations, two stages of CBM production are selected to perform the fluid substitution: 1) Initial state assuming 100% of brine saturation and 2) after 8 years of depletion with 82% of brine saturation and 18% of methane saturation. A Gassmann fluid substitution is performed to determine changes in  $V_p$ ,  $V_s$  and density due to the variation of fluid saturations in the porous space. Finally, the estimated values of  $V_p$ ,  $V_s$  and density for two stages of CBM production are used to generate synthetic seismograms using a 30 Hz and a 60 Hz Ricker wavelet and different coalbed thicknesses. Three cases are represented in the synthetic seismograms to evaluate the resolution limits of the seismic response: Corbett Field case (Main seam of 3.65 m and Lower seam of 1.67 m), a coal seam of 10.64 m of thickness and a 21.28 m coal seam.

In the Case I, two coalbed seams, as occurs in the Corbett Field, are evaluated in the synthetic seismograms. In this case, using a 60 Hz Ricker wavelet, the seismic resolution is not enough to resolve the two seams separately and there is only evidence of a small change in amplitude after fluid substitution. In the second case, involving a 10.64 m

coalbed, the top and the base of the coal seam are identified with the 30 Hz and the 60 Hz Ricker wavelet and also a change in the character of the wavelet is observed after replacing brine by methane in the porous space. For a 21.28 m coalbed the coal seam was resolved and accentuated changes in amplitude and phase occur after fluid substitution.

In this study it was necessary at least a 10 m coalbed to be able to resolve it and observe representative changes in the seismic response due to the replacement of brine by methane. Also, in terms of AVO it was observed that there is decrease of the amplitude with offset caused by the presence of methane in the pore space.

## **5.2 Evaluation of Elastic Impedance and Elastic Impedance Coefficient as a monitoring tool during CO<sub>2</sub>-ECBM production**

An impedance analysis is performed in Chapter 4 of this thesis in order to determine if it is possible to discriminate CO<sub>2</sub> from methane in coalbeds by estimating the Elastic Impedance (EI) and Elastic Impedance Coefficient (EC) attributes. To perform this task, a similar methodology to the one applied in Chapter 3 is implemented but in this case, a data set from the Fruitland Formation coals is used.

The fluid simulation gives us important information about the distribution of CO<sub>2</sub>, methane and brine in the area of study as well as of the saturation of each of them. The fluid simulation show the movement of the CO<sub>2</sub> during and after injection into the coalbed. During CO<sub>2</sub> injection, the CO<sub>2</sub> plume presents a radial distribution in the coalbed and after the injector wells are shut the CO<sub>2</sub> plume seems to be displacing to the south of the area of study, where the lower pressure are present.

The changes in  $V_p$  obtained from the Gassmann fluid substitution, after replacing brine by methane, were a decrease around 55 m/s for the primary production case and

around 65 m/s by 2011, after finishing CO<sub>2</sub> injection. The movement of the CO<sub>2</sub> flood can be appreciated in the velocity maps and it is associated to a decrease in  $V_p$ .

In the case of the  $V_s$  and density, it is possible to identify the CO<sub>2</sub> flood but in this case, the changes present a small magnitude and are not significant.

Attributes like Elastic Impedance and Elastic Impedance Coefficient, are used as tools to attempt the discrimination of CO<sub>2</sub> and methane saturated coalbeds, as well as the monitoring of the CO<sub>2</sub> injected flood. In this case, Elastic Impedance and Elastic Impedance Coefficient are not able to completely differentiate the presence of CO<sub>2</sub> and methane but it is possible to monitor the movement of the CO<sub>2</sub> flood during and after injection. The changes due to CO<sub>2</sub> injection are evident in EI and EC but the last one tends to highlight the CO<sub>2</sub> effect over the other changes in impedance in the area.

The changes in EI and EC that are appreciated are small and it is difficult to determine if these changes are going to be evident in seismic data.

## References

- Alpern B., and Lemos de Sousa M.J. 2002. Documented international enquiry on solid sedimentary fossil fuels; coal: definitions, classifications, reserves- resources, and energy potential. *International Journal of Coal Geology* 50, 3-41
- Bachu S. 2007. Carbon dioxide storage capacity in uneconomic coal beds in Alberta, Canada. Methodology, potential and site identification. *International Journal of Greenhouse gas control I*, 374-385
- Balan H.O., and Gumrah F. 2009. Enhanced coalbed methane recovery with respect to physical properties of coal and operational parameters. *Journal of Canadian Petroleum Technology* 48, 56-61
- Banerjee I., and Goodarzi J. 1990. Paleoenvironmental and sulphur-boron contents of the Mannville (Lower Cretaceous) coals of the southern Alberta, Canada. *Sedimentary Geology* 67, 297-310
- Batzle M., and Wang Z. 1992. Seismic properties of pore fluids. *Geophysics* 57, 1396-1408
- Beaton A. 2003. Production Potential of Coalbed Methane Resources in Alberta. Alberta Geological Survey. EUB/AGS Earth Science Report 2003-03
- Beaton A., Langenberg W., and Pana C. 2006. Coalbed methane resources and reservoir characteristics from the Alberta Plains, Canada. *International Journal of Coal Geology* 65, 93-113
- Beaton A., Pana C., Chen D., Wynne D., and Langenberg C.W. 2002. Coalbed Methane Potential of Upper Cretaceous-Tertiary strata, Alberta Plains. Alberta Geological Survey. EUB/AGS Earth Science Report 2002-06
- Bell G., and Rakop K. 1986. Hysteresis of methane/coal sorption isotherms. SPE Annual Technical Conference and Exhibition, New Orleans, Louisiana, USA, SPE15454
- Bradley J.S., and Powley D.E. 199. Pressure Compartments in Sedimentary Basins: A Review. AAPG Memoir, American Association of Petroleum, P. Ortoleva (ed.), Tulsa, Oklahoma, 3-26
- Busch A., and Gensterblum Y. 2011. CBM and CO<sub>2</sub>-ECBM related sorption processes in coal: a review. *International Journal of Coal Geology* 87, 49-71

- Byrnes T.L., and Schuldhaus K.F. 1995. Coalbed methane in Alberta. *The Journal of Canadian Petroleum Technology* 34, 57-62
- Chakhmakhchev A. 2007. Worldwide coalbed methane overview. SPE Hydrocarbon Economics and Evaluation Symposium, Dallas, Texas, SPE 106850-MS
- Cao H., Yang Z., and Li Y. 2008. Elastic Impedance Coefficient (EC) for Lithology Discrimination and Gas Detection. SEG Las Vegas Annual Meeting, SGA001526
- Chen Z., Liu J., Elsworth D., Connell L., and Pan Z. 2009. Investigation of CO<sub>2</sub> injection induced coal-gas interactions. 43rd U.S. rock Mechanics Symposium & 4th U.S Canada Rock Mechanics Symposium, June 28-July 1, paper 09-099
- Clarkson C. 2003. Application of a new multicomponent gas adsorption model to coal gas adsorption systems. *SPE Journal* 8, 236-251
- Clarkson C., and Bustin R.M. 2000. Binary gas adsorption/desorption isotherms: effect of moisture and coal composition upon carbon dioxide selectivity over methane. *International Journal of Coal Geology* 42, 241-271
- Clarkson C., and Bustin R.M. 2010. Coalbed Methane: Current Evaluation Methods, Future Technical Challenges. SPE Unconventional Gas Conference, Pittsburgh, Pennsylvania, USA, SPE 131791-MS
- Clarkson C., Pan Z., Palmer I., and Harpalani S. 2010. Predicting sorption-induced strain and permeability increase with depletion for coalbed methane reservoirs. *SPE Journal* 15, 152-159
- Cockbill J.R., Finn C.M., and Krawiec M.B. 2008. Economics of Mannville CBM Development: Drilling & Production Innovation at Corbett Creek. Canadian International Petroleum Conference Paper 2008-200
- Connolly P. 1999. Elastic Impedance. *The Leading Edge* 18, 438-452
- Crist T.E., Boyer C.M., and Kelso B.S. 1989. A Geologic and Coalbed Methane Resource Analysis of the Menefee Formation in the San Juan Basin, Southwestern Colorado and Northwestern New Mexico. Low Permeability Reservoirs Symposium, 00018945-MS

- Cui X., and Bustin R.M. 2005. Volumetric strain associated with methane desorption and its impact on coalbed gas production from deep coal seams. *American Association of Petroleum Geologists bulletin* 89, 1181–1202
- De Silva P.N.K., Ranjith P.G., and Choi S.K. A study of methodologies for CO<sub>2</sub> storage capacity estimation of coal. *Fuel* 91, 1-15
- Deisman N., Ivars D., Darcel C., and Chalaturnyk R. 2009. Empirical and numerical approaches for geomechanical characterization of coal seam reservoirs. *International Journal of Coal Geology* 82, 204-212
- Dvorkin J., Mavko G., and Gurevich B. 2007. Fluid substitution in shaley sediment using effective porosity. *Geophysics* 72, 1-8
- Duffaut K., Alsos T., Landro M., Rogno H., and Al-Najjar N. 2000. Shear-wave elastic impedance. *The Leading Edge* 19, 1222-1229
- Finn C., Cockbill J.R., Seely D., and Martin J. 2010. Maximum reservoir contact wells for coalbed methane exploitation: Corbett Creek case study. *Annual AAPG Convention Abstracts* 19, 49
- Flaim S.J., Hemphill R.C., and Cohn J.E. 1987. Economic factors affecting the rate of development of coalbed methane resources. SPE 18564-MS
- Gassmann, F. 1951. Über die elastizität poröser medien: *Vierteljahrsschrift der Naturforschenden Gesellschaft in Zurich* 96, 1-23. Paper translation at <http://sepwww.stanford.edu/sep/berryman/PS/gassmann.pdf>
- Gatens M. 2005. Coalbed methane development: Practices and progress in Canada. *Journal of Canadian Petroleum Technology* 44, 16-21
- Gentz T., and Bolen D. 2008. The use of numerical simulation in predicting coalbed methane producibility from Gates coals, Alberta Inner Foothills, Canada: Comparison with Mannville coal CBM production in the Alberta Syncline. *International Journal of Coal Geology* 74, 215-236
- Gentz T., Goodarzi F., Cheung F.K., and Laggoun-Defarge F. 2008. Coalbed methane producibility from the Mannville coals in Alberta, Canada: A comparison of two areas. *International Journal of Coal Geology* 74, 237-249

- Gorucu F.B., Jikich S.A., Bromhal G.S., Sams W.N., Ertekin T., and Smith D.H. 2007. Effects of matrix shrinkage and swelling on the economics of enhanced-coalbed-methane production and CO<sub>2</sub> sequestration in coal. *SPE Reservoir Evaluation & Engineering* 10, 382-392
- Gu F., and Chalaturnyk R.J. 2006. Numerical simulation of stress and strain due to gas sorption/desorption and their effects on in situ permeability of coalbeds. *Journal of Canadian Petroleum Technology* 45, 52-62
- Han D., and Batzle M. 2004. Gassmann's equation and fluid-saturation effects on seismic velocities. *Geophysics* 69, 398-405
- Jenkins C., DeGolyer, MacNaughton, and Boyer C. 2008. Coalbed and Shale Gas Reservoirs. *Journal of Petroleum Technology* 60, 92-99
- Jones A., Ahmed U., Bush D., Holland M., Kelkar S.M., Rakop K.C., Bowman K.C., and Bell G.J. 1984. Methane Production Characterization for a Deeply Buried Coalbed Reservoir in the San Juan Basin. *Unconventional Gas Recovery Symposium, SPE/DOE/GRI 12876*
- Kaiser W.R., and Ayers W.B. 1994. Geologic and Hydrologic Characterization of Coalbed Methane Reservoirs in the San Juan Basin. *SPE Formation Evaluation* 9, 175-184
- Karacan O. 2007. Swelling-induced volumetric strains internal to a stressed coal associated with CO<sub>2</sub> sorption. *International Journal of Coal Geology*. 72, 209-230
- Kopera G., Oudinot A., McColpin G., Liu N., Heath J., Wells A., and Young G. 2009. CO<sub>2</sub>-ECBM/Storage Activities at the San Juan Basin's Pump Canyon Test Site. *SPE Annual Technical Conference and Exhibition, SPE 124002*
- Kopera G., and Riestenberg D. 2009. Carbon dioxide enhanced coalbed methane and storage: is there promise?. *SPE International conference on CO<sub>2</sub> Capture, Storage, and Utilization, San Diego, California, USA, SPE 126627-MS*
- Kumar D. 2006. A tutorial on Gassmann Fluid Substitution: Formulation, Algorithm and Matlab Code. *Geohorizons* 11, 4-12
- Laubach S.E., and Tremain C.M. 1991. Regional coal fracture patterns and coalbed methane development. *The 32nd U.S. Symposium on Rock Mechanics (USRMS), ISBN 90 6191 194X*

- Lespinasse D.J., and Ferguson R.J. 2011. Fluid substitution in coalbeds. *Canadian Journal of Exploration Geophysics* 36, 17-35
- Lespinasse D.J., Clarkson C.R., and Ferguson R.J. 2012. Impedance analysis for methane and CO<sub>2</sub> discrimination in coalbeds. *Canadian Journal of Exploration Geophysics* (under review)
- Lin W., Tanq G.-Q., and Kovscek A.R. 2008. Sorption-induced permeability change of coal during gas-injection processes. *SPE Reservoir Evaluation & Engineering* 11, 792-802
- Magill D., Ramurthy M., Jordan J., and Nguyen P. 2010. Controlling Coal-Fines Production in Massively Cavitated Openhole Coalbed-Methane Wells. *SPE Asia Pacific Oil and Gas Conference and Exhibition*, SPE 134031-MS
- Marvor J., and Gunter W. 2006. Secondary porosity and permeability of coal vs. gas composition and pressure. *SPE Reservoir Evaluation & Engineering* 9, 114-125
- Mavko G., Mukerji T., and Dvorkin J. 2009. *The rock physics handbook*. Cambridge, Second Edition
- Mazumder S., and Wolf K.H. 2008. Differential swelling and permeability change of coal in response to CO<sub>2</sub> injection for ECBM. *SPE Asia Pacific Oil and Gas Conference and Exhibition*, Perth, Australia, SPE 114791-MS
- McCrank J., and Lawton D. 2009. Seismic characterization of a CO<sub>2</sub> flood in the Ardley coals, Alberta, Canada. *The Leading Edge* 28, 820-825
- Meany K., Paterson L. 1996. Relative permeability in coal. *SPE Asia Pacific Oil & Gas Conference*, Adelaide, Australia, SPE Paper 36986
- Michael E., Anders D., and Law B. 1993. Geochemical evaluation of Upper Cretaceous Fruitland Formation coals, San Juan Basin, New Mexico and Colorado. *Organic Geochemistry* 20, 475-498
- Mitra A., and Harpalani S. 2007. Modeling incremental swelling of coal matrix with CO<sub>2</sub> injection in coalbed methane reservoirs. *Eastern Regional meeting*, 17-19 October 2007, Kentucky USA, SPE 111184-MS
- Morad K., Mireault R., and Dean L. 2008. Coalbed methane fundamentals. *Reservoir* 9, 23-26

- Odeh A. 1969. Reservoir Simulation...What is it? *Journal of Petroleum Technology* 21, 1383-1388
- Oudinot A., Koperna G., Philip Z., Liu N., Heath J., Wells A., Young G., and Wilson T. 2009. CO<sub>2</sub> Injection Performance in the Fruitland Coal Fairway, San Juan Basin: Results of a Field Pilot. SPE International Conference on CO<sub>2</sub> Capture, Storage, and Utilization, SPE International Conference on CO<sub>2</sub> Capture, Storage, and Utilization, San Diego, California, USA, SPE 127073-MS
- Palmer I. 2009. Permeability changes in coal: Analytical modeling. *International Journal of Coal Geology* 77, 119–126
- Palmer I., and Mansoori J. 1998. How Permeability Depends on Stress and Pore Pressure in Coalbeds: A New Model. *SPE Reservoir Evaluation & Engineering* 1, 539-544
- Pan Z., and Connell D. 2009. Comparison of adsorption models in reservoir simulation of enhanced coalbed methane recovery and CO<sub>2</sub> sequestration. *International journal of greenhouse gas control* 3, 77-89
- Pashin, J. 1998. Stratigraphy and structure of coalbed methane reservoirs in the United States: An overview. *International Journal of Coal Geology* 35, 209-240
- Peng S., Chen H., Yang R., Gao Y., and Chen X. 2006. Factors facilitating or limiting the use of AVO for coal-bed methane. *Geophysics* 71, 49-56
- Ramos A., and Davis T. 1997. 3-D AVO analysis and modeling applied to fracture detection in coalbed methane reservoirs. *Geophysics* 62, 1683-1695
- Robertson E.P. 2008. Improvements in measuring sorption-induced strain and permeability. SPE Eastern Regional / AAPG Eastern Section Joint Meeting, Pittsburgh, Pennsylvania, USA, SPE 116259
- Robertson E.P., and Christiansen R.L. 2008. A permeability model for coal and other fractured, sorptive-elastic media. *SPE Journal* 13, 314-324
- Shi J., and Durucan S. 2005. A model for changes in coalbed permeability during primary and enhanced methane recovery. *SPE Reservoir Evaluation & Engineering* 8, 291-299
- Smith T., Sondergeld C., and Rai C. 2003. Gassmann fluid substitution: A tutorial. *Geophysics* 68, 430-440

- Snyder G., Riese W., Franks S., Fehn U., Pelzmann W., Gorody A., and Moran J. 2003. Origin and history of waters associated with coalbed methane:  $^{129}\text{I}$ ,  $^{36}\text{Cl}$ , and stable isotope results from the Fruitland Formation, CO and NM. *Geochimica et Cosmochimica Acta* 67, 4529-4544
- Vandamme M., Brochard L., Lecampion B., and Coussy O. 2010. Adsorption and strain: The  $\text{CO}_2$ -induced swelling of coal. *Journal of the mechanics and physics of solids* 58, 1489-1505
- Whitcombe D. 2002. Elastic Impedance normalization. *Geophysics* 67, 60-62
- Whitcombe D., Connolly P., Reagan R., and Redshaw T. 2002. Extended elastic impedance for fluid and lithology prediction. *Geophysics* 67, 63-67
- Yu G., Keeva V., and Durney D. 1993. The influence of confining pressure and water saturation on dynamic elastic properties of some Permian coals. *Geophysics* 58, 30-38
- Zarantonello S., Bevc D., and Harris J. 2010. Integrated reservoir, petrophysical, and seismic simulation of  $\text{CO}_2$  storage in coal beds. *The Leading Edge* 29, 184-190